IOP PUBLISHING REPORTS ON PROGRESS IN PHYSICS

Rep. Prog. Phys. **72** (2009) 016502 (25pp) doi:10.1088/0034-4885/72/1/016502

Electron energy-loss spectroscopy in the TEM

R F Egerton

Physics Department, University of Alberta, T6G 2G7 Canada

E-mail: egerton@phys.ualberta.ca

Received 15 August 2008, in final form 18 November 2008
Published 16 December 2008
Online at stacks.iop.org/RoPP/72/016502

Abstract

Electron energy-loss spectroscopy (EELS) is an analytical technique that measures the change in kinetic energy of electrons after they have interacted with a specimen. When carried out in a modern transmission electron microscope, EELS is capable of giving structural and chemical information about a solid, with a spatial resolution down to the atomic level in favourable cases. The energy resolution is typically 1 eV but can approach 0.1 eV if an electron-beam monochromator is used. This review provides an overview of EELS instrumentation and of the physics involved in the scattering of kilovolt electrons in solids. Features of the energy-loss spectrum are discussed, including plasmon peaks, inner-shell ionization edges and fine structure related to the electronic densities of states. Examples are given of the use of EELS for the measurement of local properties, including specimen thickness, mechanical and electronic properties (such as bandgap) and chemical composition. Factors that determine the spatial resolution of the analysis are outlined, including radiation damage to the specimen. Comparisons are made with related techniques, particularly x-ray absorption spectroscopy.

(Some figures in this article are in colour only in the electronic version)

This article was invited by Professor D Cockayne.

Contents

1. Introduction

Electron energy-loss spectroscopy (EELS) involves measurement of the energy distribution of electrons that have interacted with a specimen and lost energy due to inelastic scattering. If the incident electrons have a kinetic energy of a few hundred electron volts and are reflected from the surface of the specimen, the technique is called high-resolution EELS (HREELS). Relatively simple instrumentation can then provide spectra with an energy resolution down to a few millielectron volts, sufficient to resolve vibrational as well as electronic modes of energy loss; this technique is used

extensively for studying the physics and chemistry of solid surfaces (Ibach and Mills 1982).

This paper is not about HREELS but about spectroscopy employing higher energy electrons, typically 100–300 keV, as used in a transmission electron microscope (TEM). Because of their greater energy, such electrons can pass completely through a specimen, provided its thickness is below about 1 μm. The electromagnetic lenses of the TEM can be used to focus them into a 'probe' of very small diameter (1 nm or even 0.1 nm) or to produce a transmitted-electron image of the specimen, with a spatial resolution down to atomic dimensions. As a result, EELS carried out in a TEM is capable of very high spatial resolution. Combined with the low specimen thickness, this implies spectroscopic analysis of extremely small volumes of material.

For comparison, x-ray absorption spectroscopy (XAS) currently has a lateral resolution of around 30 nm if carried out using synchrotron radiation focused by a zone plate. Owing to the weaker interaction of photons with matter, XAS uses a thicker specimen, which is sometimes an advantage since it allows easier specimen preparation. Also, XAS can examine a specimen surrounded by air or water vapour, whereas the TEM usually places the specimen in a high vacuum.

Much of the spectral information obtainable from EELS is similar to that given by synchrotron-XAS, so the TEM-EELS combination has been referred to as a synchrotron in a microscope (Brown 1997). Because EELS can be combined with transmission imaging, electron diffraction and x-ray emission spectroscopy, all in the same instrument, the technique has become important for studying the physics and chemistry of materials.

Figure 1(a) shows a typical energy-loss spectrum, recorded up to a few tens of electron volts, sometimes called the low-loss region. The first peak, the most intense for a very thin specimen, occurs at 0 eV and is therefore called the zero-loss peak. It represents electrons that did not undergo inelastic scattering (interaction with the electrons of the specimen) but which might have been scattered elastically (through interaction with atomic nuclei) with an energy loss too small to measure. The width of the zero-loss peak, typically 0.2–2 eV, reflects mainly the energy distribution of the electron source.

Other low-loss features arise from inelastic scattering by conduction or valence electrons. The most prominent peak, centred around 22 eV in figure 1(a), results from a plasma resonance of the valence electrons. The increase in intensity around 54 eV represents inelastic scattering from inner-shell electrons, in this case the M_2 and M_3 subshells ($3p^{1/2}$ and $3p^{3/2}$ electrons) of iron atoms. Its characteristic shape, a rapid rise followed by a more gradual fall, is termed an ionization edge; it is the exact equivalent of an absorption edge in XAS. Other ionization edges occur at a higher energy loss in figure 1(b): a fluorine K-edge (excitation of 1s electrons) followed by iron L_3 and L_2 edges (representing excitation of Fe $2p^{3/2}$ and $2p^{1/2}$ electrons). Before discussing how these various features provide us with information about the specimen, we will briefly examine the principles and instrumentation involved in obtaining energy-loss spectra in the TEM.

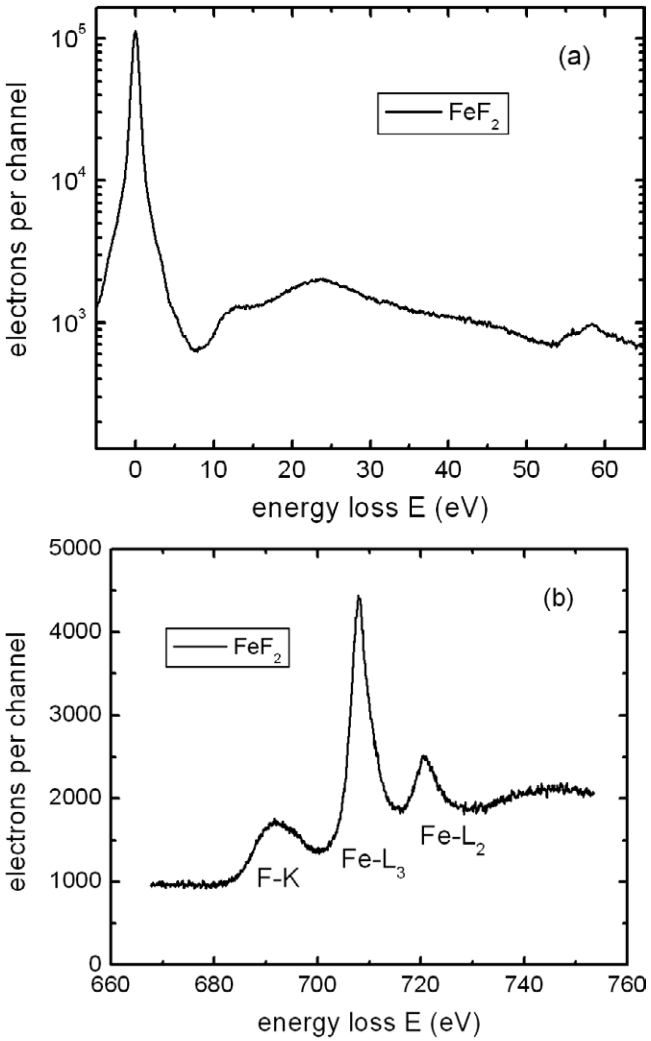

Figure 1. Energy-loss spectrum of an iron fluoride film: (a) low-loss region with a logarithmic intensity scale and (b) part of the core-loss region, with linear vertical scale. Courtesy of Feng Wang, National Institute for Nanotechnology, Edmonton, Canada.

2. Instrumentation

TEM-EELS instrumentation is based on the magnetic prism, in which a uniform magnetic field B (of the order of 0.01 T) is generated by an electromagnet with carefully shaped polepieces; see figure 2. Within this field, electrons follow circular paths of radius R and are deflected through an angle of typically 90°. The sideways force on an electron is $F = Bev = mv^2/R$ where, e, v and m are the electron speed, charge and relativistic mass, giving a bend radius that depends on speed and therefore on electron energy:

$$R = (m/e)(1/B)v. \tag{1}$$

While this behaviour resembles the bending and dispersion of a beam of white light by a glass prism, the electron prism also has a focusing action. Electrons that stray from the central trajectory (the optic axis) in a direction perpendicular to the field (figure 2(a)) experience an increase or decrease in their path length within the field, giving rise to a greater or lesser deflection angle. If the entrance beam originates

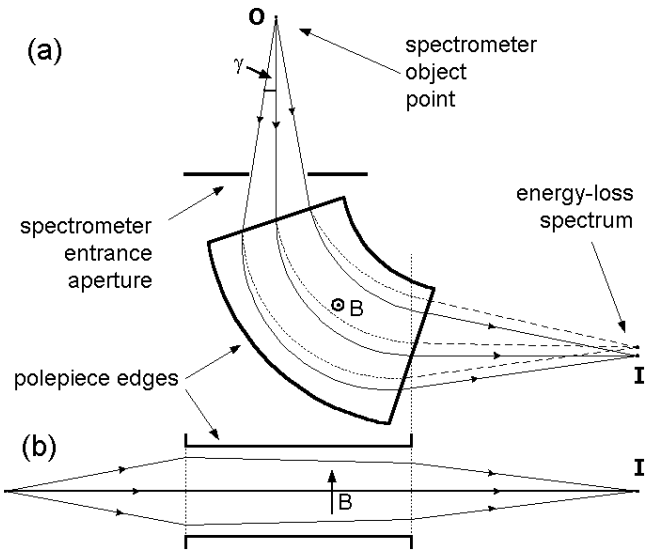

Figure 2. Dispersive and focusing properties of a magnetic prism (*a*) in a plane perpendicular to the magnetic field and (*b*) parallel to the field. Solid lines represent zero-loss electrons ($E = 0$); dashed lines represent those that have lost energy during transmission through the specimen.

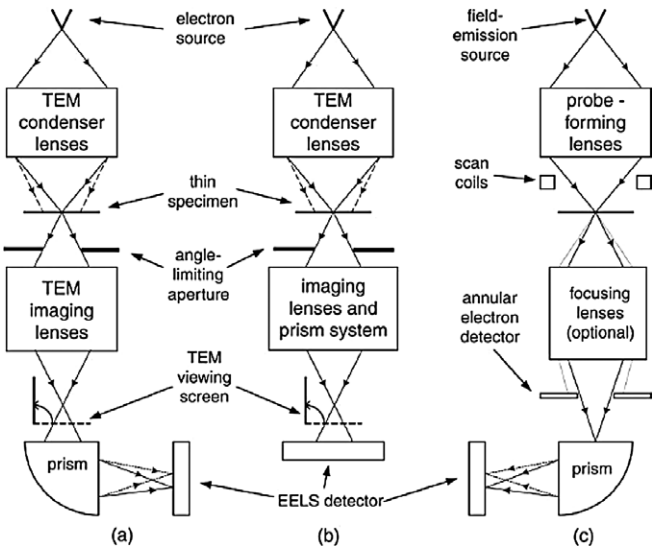

Figure 3. Three procedures for TEM-based energy-loss spectroscopy: (*a*) conventional TEM with a magnetic-prism spectrometer below the viewing screen, (*b*) TEM incorporating an in-column imaging filter and (*c*) scanning-transmission (STEM) system.

from a point object, electrons of a given energy are returned to a single image point. The existence of different electron energies then results in a focused spectrum in a plane passing through that point. In addition, the fringing field at the polepiece edges focuses electrons that deviate in a direction y parallel to the magnetic field (figure 2(*b*)). By adjusting the angles of the polepiece edges, the focusing power in these two perpendicular directions can be made equal (double-focusing condition), giving a spectrum of small width in the direction of the applied magnetic field. As a result of second-order aberrations, the focusing is imperfect but these aberrations can be corrected by curving the polepiece edges, allowing an energy resolution better than 1 eV for an entrance angle of up to several milliradians (of the order of 0.3°).

The simplest form of energy-loss system consists of a conventional TEM fitted with a magnetic prism below its image-viewing chamber (figure 3(*a*)). By tilting the TEM screen to a vertical position, electrons are allowed to enter the spectrometer, where they are dispersed according to their kinetic energy, which is their incident energy E_0 minus any energy loss E occurring in the specimen. The spectrometer object point is an electron-beam crossover produced just below the bore of the final (projector) TEM lens. A spectrometer entrance aperture, typically variable from 1 to 5 mm in diameter, limits the range of entrance angles and ensures adequate energy resolution. This kind of system requires little or no modification of the TEM, which operates according to its original design and specification.

An alternative strategy is to incorporate a spectrometer into the TEM imaging column (figure 3(*b*)). For image stability, it is important to preserve a vertical TEM column, so there are usually four magnetic prisms that bend the beam into the shape of a Greek letter Ω, hence the name 'omega filter'. An energy-loss spectrum is produced just below the filter and subsequent TEM lenses project it onto the viewing screen or onto an electronic detector, usually employing a CCD camera. Alternatively, these lenses may focus a plane (within the spectrometer) that contains an image of the specimen, utilizing the imaging properties of a magnetic prism. A narrow slit inserted at the spectrum plane can remove all electrons except those within a small energy window, resulting in an energy-filtered (EFTEM) image on the TEM screen or the CCD camera. Provided its image aberrations are corrected by quadrupole and sextupole lenses, the post-column magnetic prism (figure 3(*a*)) can also produce EFTEM images, as in the GIF spectrometer marketed by the Gatan Company.

A third type of system (figure 3(*c*)) is based on the scanning-transmission electron microscope (STEM), in which a field-emission source and strong electromagnetic lenses are used to form a small probe that can be raster-scanned across the specimen. A dark-field image, representing transmitted electrons scattered through relatively large angles, is formed by feeding the signal from a ring-shaped (annular) detector to a display device scanned in synchronism with the probe scan. Electrons scattered through smaller angles enter a single-prism spectrometer, which produces an energy-loss spectrum for a given position of the probe on the specimen (Browning *et al* 1997). Inserting a slit in the spectrum plane then gives an energy-filtered image, obtained this time in serial mode. Alternatively, the whole spectrum is read out at each probe position (pixel), resulting in a large spectrum-image data set that can be processed off-line (Jeanguillaume and Colliex 1989). Similar data can be obtained from an EFTEM system (figure 3(*b*)) by recording a sequence of EFTEM images of different energy loss, selected by changing the spectrometer current or the microscope high voltage.

Although energy-loss spectra were originally recorded by placing a photographic film at the spectrum plane, this arrangement soon gave way to electronic acquisition. In a serial-recording system, a narrow slit is placed in the

spectrum plane and the spectrum scanned past the slit by varying the magnetic field of the prism or the microscope high voltage; raising the voltage selects a higher energy loss, for a given slit position. A single-channel electron detector behind the slit produces an electrical signal proportional to the electron intensity at each energy loss; it usually consists of a scintillator, to convert the electrons to visible photons, and a photomultiplier tube that acts as a high-sensitivity photon detector. This simple system works well but provides noisy data at high-energy loss, where the electron intensity is weak. The reason lies not in the photomultiplier tube, which is a low-noise detector, but in the fact that only a small range of energy loss is sampled at any instant, resulting in pronounced shot noise due to the limited number of electrons being recorded.

To facilitate recording higher energy losses, parallel-recording detectors were developed. They contain no energy-selecting slit, so no electrons are wasted. An extended range of the energy-loss spectrum is projected by an electron lens onto a fluorescent screen, coupled to a CCD camera whose output is fed into the data-recording computer. Although this procedure has largely replaced serial recording, it gives spectral peaks with extended tails that arise from light scattering in the fluorescent screen. These tails can be removed by spectrum processing (deconvolution) or minimized by using a high spectral dispersion (although this limits the energy range of the data).

The energy resolution of an energy-loss spectrum is determined by several factors, including aberrations of the electron spectrometer. By curving the polepieces of the magnetic prism and by using weak multipole lenses for fine tuning, these aberrations can be almost eliminated. The energy resolution is then determined by the width of the energy distribution provided by the electron source, seen as the width of the zero-loss peak. Thermionic sources, such as the tungsten filament or heated LaB_6 source used in many electron microscopes, provide an energy width between 1 and 2 eV. A Schottky source (heated Zr-coated W tip) gives a width of about 0.7 eV. A CFEG source (field-emission from a cold tungsten tip) gives typically 0.5 eV, although a fast readout of the spectrum combined with software re-alignment can reduce this width to below 0.3 eV (Kimoto and Matsui 2002, Nehayah *et al* 2007).

Further improvement in energy resolution is possible by inserting an electron monochromator after the electron source. The monochromator is an energy filter tuned to a narrow energy band at the centre of the emitted-energy distribution. Although either magnetic-prism or electrostatic-prism designs are possible, a popular choice is the Wien filter, which uses both electric and magnetic fields and results in an energy spread of about 0.2 eV (Tiemeijer 1999).

Another recent development is the correction of TEM-lens aberrations by multipole lenses that are adjusted and aligned under computer control. Used to correct the spherical aberration of a probe-forming lens (e.g. the objective lens of a STEM), the corrector allows electrons to be focused into a probe of diameter below 0.1 nm (Krivanek *et al* 1999). Similar techniques can be used to correct the spherical and chromatic aberration of the first imaging lens (objective) of a conventional TEM (Haider *et al* 1998). Although subatomic resolution might seem unnecessary, it greatly assists the atomic-scale analysis of individual defects in crystalline materials.

3. The physics of EELS

When electrons pass through a specimen, they are scattered (changed in direction) by interaction with atoms of the solid. This interaction (or collision) involves electrostatic (Coulomb) forces, arising from the fact that the incident electron and the components of an atom (nucleus and atomic electrons) are all charged particles. For convenience we can divide the scattering into elastic and inelastic, depending on whether or not the incident electron responds to the field of the nucleus or to its surrounding electrons.

3.1. Elastic scattering

Elastic scattering involves the interaction of an incident electron with an atomic nucleus. Because the nuclear mass greatly exceeds the rest mass of an electron (by a factor $1823A$ where A = atomic weight or mass number), the energy exchange is small and usually unmeasurable in a TEM-EELS system. For elastic scattering by a single atom (and in an *amorphous* material, to a first approximation) the differential cross section that represents the probability of scattering per unit solid angle Ω is (Lenz 1954)

$$\mathrm{d}\sigma_e/\mathrm{d}\Omega = [4Z^2/(k_0^2T)](\theta^2 + \theta_0^2)^{-2}. \qquad (2)$$

Here Z is the atomic number, k_0 is the electron wavenumber (2π/wavelength) and T is a 'nonrelativistic' incident energy given by

$$T = m_0v_0^2/2 = E_0[1 + E_0/(2m_0c^2)]/[1 + E_0/(m_0c^2)], \qquad (3)$$

where $m_0c^2 = 511\,\mathrm{keV}$ is the electron rest energy. The parameter T is somewhat less than the actual kinetic energy E_0 because the relativistic mass of the electron exceeds its rest mass m_0; see table 1. In equation (2), θ represents the scattering angle of the electron and $\theta_0 \approx Z^{1/3}/(k_0a_0)$ is the angular width of the scattering distribution, a_0 being the first Bohr radius (53×10^{-12} m). For $Z = 6$ and $E_0 = 100\,\mathrm{keV}$, $\theta_0 \approx 20\,\mathrm{mrad} \approx 0.35^\circ$, meaning that the angular distribution of elastic scattering is quite narrow for the incident-electron energies used in a TEM; see figure 4. To be scattered through a large angle ($\theta \gg \theta_0$), the electrons must pass very close to the nucleus; not surprisingly equation (2) then becomes the Rutherford formula for scattering of an electron from an unscreened nucleus. At smaller angles, the scattered intensity falls below the Rutherford value; the term θ_0 represents nuclear screening by the atomic electrons.

A *crystalline* specimen scatters electrons over a similar angular range but the scattering is confined to discrete angles (Bragg angles; see figure 4). The elastic scattering is then called diffraction. Because of atomic vibration, electrons can also undergo *phonon scattering*, which broadens the angular width of each Bragg beam and involves an energy transfer of the order of kT ($\approx$25 meV at $T \approx 300$ K) that is unmeasurable in a TEM-EELS system. For this reason and the fact that it

Table 1. Parameters $T = m_0v^2/2$, γT, $\gamma = m/m_0$, deBroglie wavelength λ and wavenumber $k_0 = 2\pi/\lambda$, as a function of the kinetic energy E_0 of an electron.

E_0 (keV)	T (keV)	γT (keV)	γ	λ (pm)	k_0 (nm^{-1})
30	27.6	29.2	1.059	6.98	900
100	76.8	91.8	1.196	3.70	1697
200	123.6	171.9	1.391	2.51	2505
300	154.1	244.5	1.587	1.97	3191
1000	226.3	669	2.957	0.87	7205

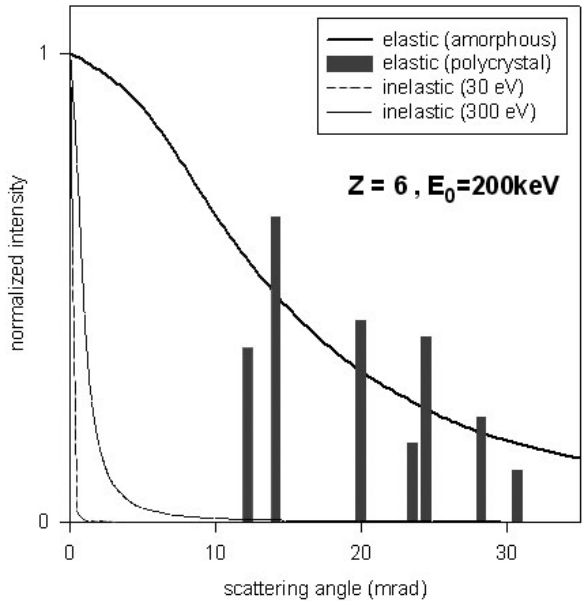

Figure 4. Curves show the angular distribution of elastic and inelastic scattering, calculated for 200 keV electrons in amorphous carbon. Vertical bars represent the relative intensities of the elastic Bragg beams in crystalline diamond when the crystal axes are parallel to the incident beam.

involves interaction with atomic nuclei, phonon scattering is often termed quasi-elastic.

For the small fraction of incident electrons that are scattered through large angles, elastic scattering does involve an appreciable energy transfer E given by

$$E = E_{\max} \sin^2(\theta/2). \tag{4}$$

For the extreme case of 180° backscattering, $E = E_{\max} \approx E_0/(457\,\text{A}) \approx 18\,\text{eV}$ for a carbon atom and $E_0 = 100\,\text{keV}$. If E_0 is several hundred kilo-electron volts, this 'elastic' scattering can be sufficient to displace an atom from its lattice site in a crystal, giving rise to a form of radiation damage called *knock-on* or *displacement* damage.

3.2. Inelastic scattering

Coulomb interaction between the incident electron and atomic electrons gives rise to *inelastic* scattering. Similarity in mass between the projectile (incident electron) and the target (atomic electron) allows the energy exchange (loss) to be appreciable: typically a few electron volts up to hundreds of electron volts.

For most inelastic collisions, the double-differential cross section is given by a small-angle approximation:

$$\begin{aligned} \mathrm{d}^2\sigma_\mathrm{i}/\mathrm{d}\Omega\,\mathrm{d}E &= (4\gamma^2/q^2)(R/E)(\mathrm{d}f/\mathrm{d}E) \\ &= (4a_0^2R^2/T)[(1/E)(\mathrm{d}f/\mathrm{d}E)](\theta^2+\theta_\mathrm{E}^2)^{-1}, \end{aligned} \tag{5}$$

where q is the magnitude of the scattering wavevector, $a_0 = 53 \times 10^{-12}\,\text{m}$, $R = 13.6\,\text{eV}$ (the Rydberg energy) and $\mathrm{d}f/\mathrm{d}E$ is an energy-differential *optical* oscillator strength, a function of energy loss E but not of scattering angle θ. As seen from equation (5), the angular distribution of inelastic scattering is a Lorentzian function whose half-width (at half-height) is the characteristic angle $\theta_\mathrm{E} = E/(2\gamma T)$. Although the relativistic factor γ (the fractional increase in relativistic mass of the incident electron) is greater than 1, the term γT is slightly less than the kinetic energy E_0 of the incident electrons, as shown in table 1. For an energy loss of $E = 25\,\text{eV}$, $\theta_\mathrm{E} = 0.14\,\text{mrad}$, illustrating the fact that inelastic scattering involves angles even smaller than those for elastic scattering; see figure 4.

Apart from the $1/E$ and angular terms in equation (5), which together represent a monotonic decay (E^{-1} for large θ, E^{-3} for very small θ), $\mathrm{d}f/\mathrm{d}E$ represents the energy dependence of inelastic scattering. This energy-differential oscillator strength also applies to photon-induced transitions, showing the close connection between energy-loss and optical spectra. The correspondence is only approximate: when a *photon* is absorbed, the momentum transfer corresponds to a wavenumber $q_\mathrm{p} = \omega/c = 2\pi E/(hc)$, E being the transferred energy. The momentum $hq/(2\pi)$ transferred by an inelastically scattered *electron* depends on its scattering angle; energy and momentum conservation lead to

$$q^2 = k_0^2(\theta^2 + \theta_\mathrm{E}^2). \tag{6}$$

The minimum momentum transfer corresponds to $\theta = 0$ and $q_\mathrm{min} = k_0\theta_\mathrm{E}$, so for the same energy transfer

$$q_\mathrm{min}/q_\mathrm{p} = (2\pi\gamma m_0 v/h)[E/(2\gamma T)][hc/(2\pi E)] = c/v. \tag{7}$$

Provided the incident-electron energy is at least 100 keV ($v/c \approx 0.55$) and the energy-loss spectrum is recorded using a really small angle-limiting spectrometer entrance aperture ($\beta \ll \theta_\mathrm{E}$), the transferred momentum is only a factor of 2 larger than for photon absorption. The energy-loss spectrum then reflects optical (direct) electronic transitions that obey a dipole sum rule: the angular-momentum quantum number l of the target atom must increase or decrease by one ($\Delta l = \pm 1$).

The E-dependence $\mathrm{d}f/\mathrm{d}E$ is characteristic of the specimen, hence the usefulness of EELS. We now discuss some of the mechanisms that give rise to this energy dependence.

3.3. Plasmon excitation

A prominent form of inelastic scattering in solids involves *plasmon* excitation. This phenomenon arises from the fact that outer-shell electrons (conduction electrons in a metal, valence electrons in a semiconductor or insulator) are only weakly bound to atoms but are coupled to each other by electrostatic forces; their quantum states are delocalized in the form of an energy band.

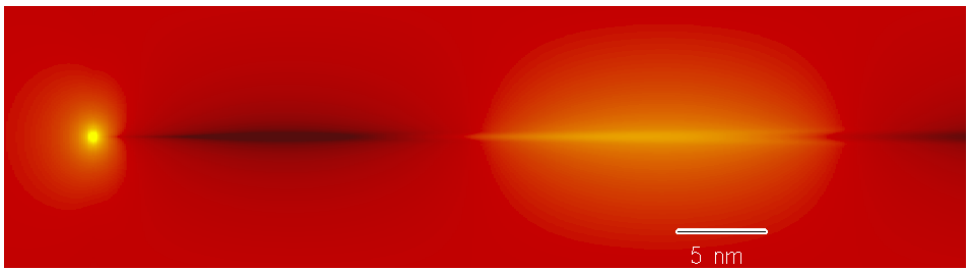

Figure 5. Plasmon wake of a 100 keV electron travelling through aluminium, calculated from the dielectric properties (P E Batson, personal communication). The electron is represented by the bright dot on the left; alternate dark and bright bands represent positive and negative regions of space charge that trail behind the electron.

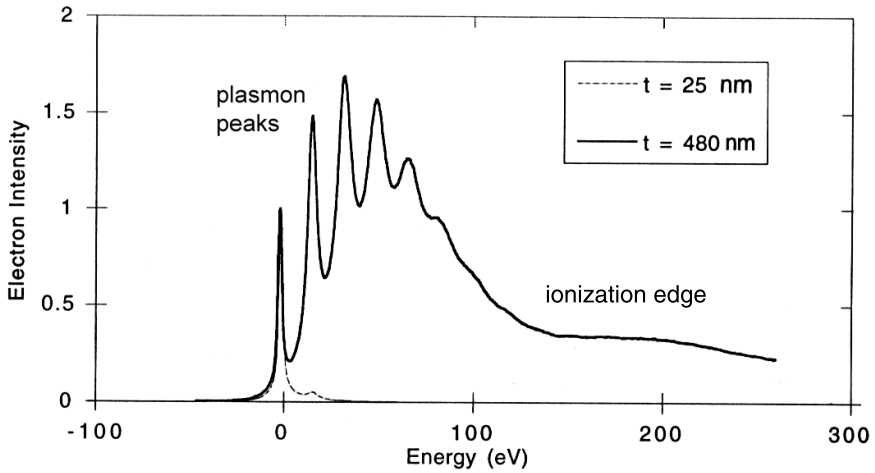

Figure 6. Energy-loss spectrum of a thin region of silicon (thin line) and of a thicker area (thick line), with their zero-loss peaks matched in height. Plasmon peaks occur at multiples of the plasmon energy ($E_p = 16.7$ eV). The broad feature starting around 100 eV is a silicon L_{23} ionization edge.

When a fast-moving electron passes through a solid, the nearby atomic electrons are displaced by Coulomb repulsion, forming a correlation hole (a region of net positive potential of size ∼1 nm) that trails behind the electron. Provided the electron speed exceeds the Fermi velocity, the response of the atomic electrons is oscillatory, resulting in regions of alternating positive and negative space charge along the electron trajectory; see figure 5. The effect is known as a *plasmon wake*, in analogy to the wake of a boat travelling on water at a speed higher than the wave velocity or an aircraft flying faster than the speed of sound. The wake periodicity in the direction of the electron trajectory is $\lambda_w = v/f_p$ where f_p is a plasma frequency given (in Hz) by

$$2\pi f_p = \omega_p = [ne^2/(\varepsilon_0 m)]^{1/2}. \tag{8}$$

Here n is the density of the outer-shell (conduction or valence) electrons and m is their effective mass. The frequency f_p is of the order of 10^{16} Hz, equivalent to the ultraviolet region of the electromagnetic spectrum.

As the electron moves through the solid, the backward attractive force of the positive correlation hole results in energy loss. The process can be viewed in terms of the creation of pseudoparticles known as *plasmons*, each of which carries a quantum of energy equal to $E_p = hf_p = (h/2\pi)\omega_p$. The inelastic scattering is then interpreted as the creation of a plasmon at each scattering 'event' of the transmitted electron, giving an energy-loss spectrum consisting of a peak at an energy loss $E = E_p$ and at multiples of that energy; see figure 6.

The probability P_n of n plasmon-loss events in a specimen of thickness t is given by Poisson statistics:

$$P_n = (1/n!)(t/L)^n \exp(-t/L), \tag{9}$$

where the plasmon *mean free path* (MFP) L is the average distance between scattering events. The integrated intensity I_n of each plasmon peak is then given by

$$I_n = P_n I_t = (1/n!)(t/L)^n \exp(-t/L) I_t = (1/n!)(t/L)^n I_0, \tag{10}$$

where I_t is the total integral of the spectrum, including its zero-loss component I_0. In the absence of elastic scattering, I_t would be the incident-beam intensity; in practice, it represents electrons that, after transmission through the specimen, are scattered through angles small enough to be accepted by the spectrometer entrance aperture (semiangle β).

The spectrometer entrance aperture also cuts off some inelastic scattering (less than the elastic because of the narrower angular distribution), reducing the inelastic intensity from I_n to $I_n(\beta)$. As a result of a fortuitous property of the Lorentzian angular distribution, $I_n(\beta)/I_n = [I_1(\beta)/I_1]^n$ to a good approximation, which allows equation (10) to be used in the presence of an angle-limiting aperture as long as L is

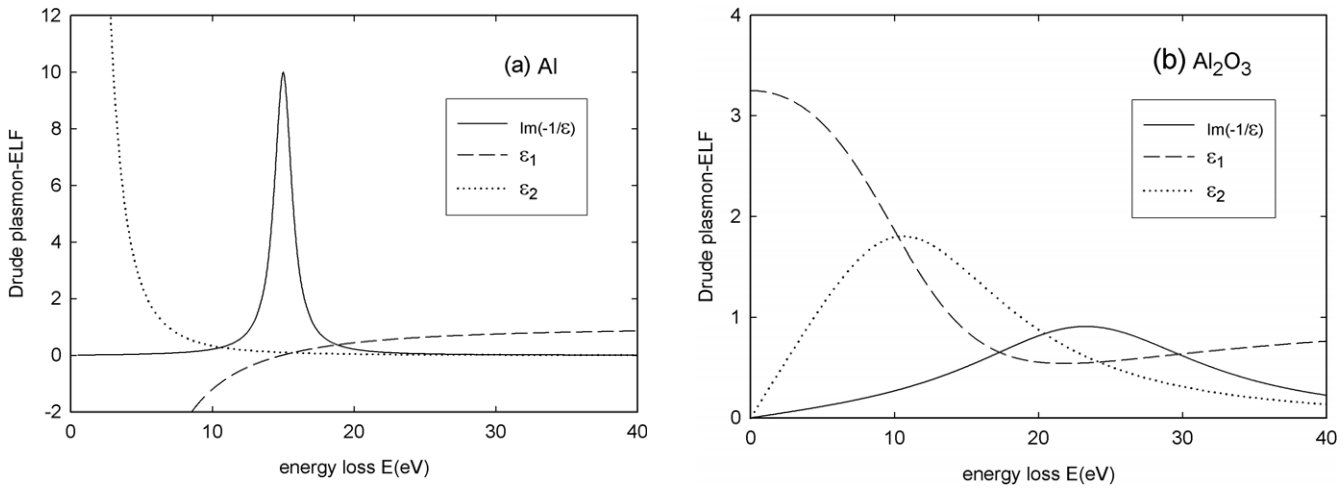

Figure 7. Permittivity and energy-loss function calculated from the Drude model for (*a*) a free-electron gas with $E_p = 15$ eV, $\Gamma = 1.5$ eV (typical of aluminium recorded by a TEM-EELS system) and (*b*) $E_p = 21$ eV, $E_b = 14$ eV, $\Gamma = 20$ eV, which gives an energy-loss function representative of amorphous Al_2O_3.

replaced by a value $L(\beta)$ that depends (logarithmically) on the spectrometer collection angle β (Egerton 1996).

Based on equation (10), the plural-scattering component of an energy-loss spectrum can be removed by *Fourier-log deconvolution* (Johnson and Spence 1974). Because of the property just discussed, this procedure is accurate even for spectra recorded with an angle-limiting aperture, provided the aperture is centred on the optic axis ($\theta = 0$). For spectra recorded off-axis (large q), more complicated procedures are necessary.

Since plasmon generation is caused by the electric field of the incident electron, a similar effect can be created by an electromagnetic wave. As a result, the energy-loss spectrum is related to the dielectric properties of the specimen. In fact, the middle term $(1/E)(\mathrm{d}f/\mathrm{d}E)$ in equation (5) can be replaced by $\mathrm{Im}[-1/\varepsilon(E)] = \varepsilon_2/(\varepsilon_1^2 + \varepsilon_2^2)$, known as the *energy-loss function*, where $\varepsilon(E)$ is a complex permittivity whose real and imaginary parts are ε_1 and ε_2. As a result of this connection, energy-loss spectra can be processed to give $\varepsilon_1(E)$ and $\varepsilon_2(E)$ data over a wide range of photon energy E, ranging from the visible to the x-ray region. The processing involves *Kramers–Kronig transformation* to get $\mathrm{Re}(1/\varepsilon)$ and various normalization procedures (Egerton 1996, Alexander *et al* 2008).

The dielectric formalism allows energy-loss spectra to be simulated. In the simple *Drude model* (Raether 1980), the outer-shell atomic electrons are approximated by a *Fermi sea* of free electrons (*jellium*) for which the complex permittivity is

$$\varepsilon = 1 - E_p^2/(E^2 + \mathrm{i}E\Gamma)$$
$$= 1 - E_p^2/(E^2 + \Gamma^2) + \mathrm{i}\Gamma E_p^2/[E(E^2 + \Gamma^2)]. \qquad (11)$$

The energy-loss function is then

$$\mathrm{Im}[-1/\varepsilon(E)] = E\Gamma E_p^2/[(E^2 - E_p^2)^2 + (E\Gamma)^2]. \qquad (12)$$

The parameter Γ represents plasmon damping and is approximately the full width at half maximum (FWHM) of the plasmon peak in the energy-loss spectrum. Equation (12) describes the shape of this peak; see figure 7(*a*). Note that for the free-electron case, the resonance peak occurs when $\varepsilon_1(E)$ is close to zero; at this energy, there is no peak in $\varepsilon_2(E)$ that would give rise to a peak in the optical-absorption spectrum.

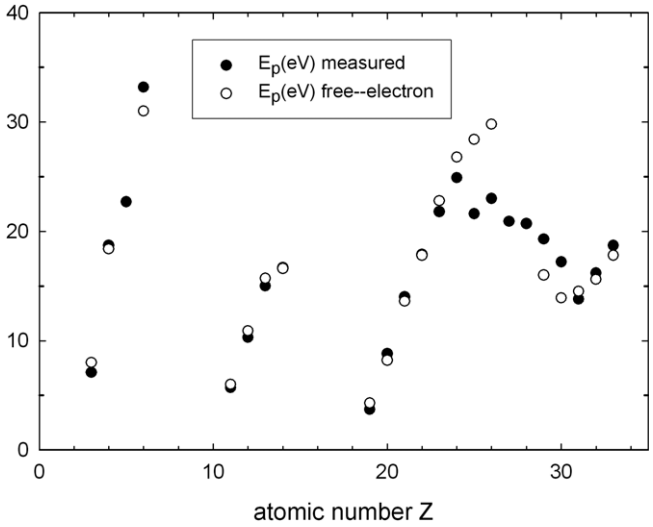

Figure 8. Plasmon energy (in eV) for elements, as measured (solid circles) and as given by the free-electron formula (open circles). Agreement is good except for the transition metals ($22 < Z < 29$), where the d-electrons contribute to an M_{23} ionization edge at higher energy loss (35–60 eV) rather than to the plasmon peak.

Except for the transition elements, whose d-electrons are not entirely free to take place in collective motion, the free-electron approximation: equation (8) with $m = m_0$, gives plasmon-peak energies quite close to those observed by EELS; see figure 8. This remains true even for semiconductors such as silicon and insulators such as diamond or alkali halides; see table 2. To take part in plasmon oscillation, the outer-shell electrons need not be capable of long-range motion (charge transport).

The Drude model can be extended to semiconductors and insulators by giving the electrons a binding energy E_b, resulting

Table 2. Measured and calculated plasmon energy, plasmon-peak width (FWHM), cutoff angle θ_c (mrad) and MFP $L_p(\theta_c)$ for $E_0 = 100$ keV.

Material	E_p (eV) measured	E_p (eV) free-electron	$h\Gamma/2\pi$ (eV) = FWHM	θ_c (mrad) $E_0 = 100$ keV	$L_p(\theta_c)$ (nm) $E_0 = 100$ keV
Al	15.0	15.8	0.5	7.7	119
Be	18.7	18.4	4.8	7.1	102
Si	16.7	16.6	3.2	6.5	115
GaAs	15.9	15.7	5.5		
MgO	22.3	24.3	6.7		
NaCl	15.5	15.7	15		

in a permittivity

$$\begin{aligned}\varepsilon &= 1 - E_p^2/(E^2 - E_b^2 + iE\Gamma)\\ &= 1 - E_p^2(E^2 - E_b^2)/[(E^2 - E_b^2)^2 + E^2\Gamma^2]\\ &\quad + iE\Gamma E_p^2/[(E^2 - E_b^2)^2 + E^2\Gamma^2],\end{aligned} \tag{13}$$

giving a plasmon peak displaced to an energy slightly higher than E_p, as illustrated for amorphous Al_2O_3 in figure 7(*b*). Note that the broad plasmon resonance now occurs at $\varepsilon_1 \approx \varepsilon_2$ and ε_1 never becomes zero or negative.

As shown in table 2, the plasmon peak represents a sharp resonance in some materials, including Al and alkali metals, and also some semiconductors such as silicon and GaAs. Other materials, such as carbon and organic compounds, show broad plasmon peaks; the peak width $h\Gamma/(2\pi)$ is large due to strong plasmon damping. Transfer of plasmon energy to individual electrons (single-electron excitation) is one cause of damping and becomes more probable at higher q, so the plasmon-peak width increases with increasing scattering angle. Damping can also increase at very small angles, due to grain-boundary scattering in a polycrystalline material (Krishnan and Ritchie 1970). The plasmon width is higher in amorphous materials (Egerton 1996); for example, 3.9 eV in amorphous silicon compared with 3.2 eV in the crystalline phase.

An n-type semiconductor has a separate plasma resonance associated with its conduction-band electrons. However, their concentration is typically below 10^{19} cm^{-2}, giving a plasmon energy below 0.25 eV, not resolvable by most TEM-EELS systems.

Carbon represents an interesting case. Assuming four valence electrons per atom, diamond has a free-electron plasmon energy of 31 eV. The measured loss spectrum shows a broad peak centred around 33 eV and about 13 eV in width, corresponding to a well-damped plasmon resonance. Graphite is a semi-metal with one weakly bound π-electron per atom, giving free-electron plasmon energy of 12.6 eV as well as a 22 eV resonance due to all four electrons. In practice, two resonance peaks are observed, at 7 and 27 eV; the resonance frequencies are forced apart due to coupling between the two groups of oscillators (Raether 1980). For single-sheet graphene, these peaks are red-shifted to 4.7 and 14.6 eV (Eberlein *et al* 2008).

Organic compounds give a broad low-loss peak, typically centred around 23 eV but with some fine structure at lower energy loss. In compounds containing double bonds, a further peak at around 6 eV is sometimes interpreted as a plasmon resonance of π-electrons. However, vapour-phase aromatic hydrocarbons show a similar peak, which must therefore be interpreted in terms of π–π^* transitions (Koch and Otto 1969). A peak in the range 6–7 eV is often taken as evidence of double bonds or an aromatic structure. Ice also shows a broad resonance around 20 eV, accompanied by a fine structure below 10 eV due to interband transitions (Sun *et al* 1993).

Plasmon dispersion means that the plasmon peak shifts to higher energy with increasing scattering angle and wavenumber, by an amount proportional to q^2. This behaviour is sometimes used to identify a spectral peak as representing a bulk (volume) plasmon, rather than single-electron excitation where the energy is expected to be independent of q.

The free-electron approximation provides a value for the MFP for plasmon excitation:

$$\begin{aligned}L_p(\beta) &\approx (4a_0T/E_p)[\ln(1 + \beta^2/\theta_{Ep}^2)]^{-1}\\ &= 8\pi a_0 T e^{-1}h^{-1}(\varepsilon_0 m_0 u A/\rho)^{1/2}z^{-1}[\ln(1 + \beta^2/\theta_{Ep}^2)]^{-1},\end{aligned} \tag{14}$$

where u is the atomic mass unit, ρ is the physical density and z is the number of quasi-free electrons per atom. The natural-logarithm term represents integration of equation (5) up to a collection angle β, taking $E \approx E_p$ such that $\theta_{Ep} = E_p/(2\gamma T)$. This term causes the MFP to decrease somewhat with increasing collection angle, by about a factor of 2 between $\beta = 1$ and 10 mrad.

In reality, equation (14) is a small-angle approximation, valid for scattering angles less than a critical angle θ_c (known as the dipole region). The wavenumber q associated with inelastic scattering is given by equation (6) and increases with scattering angle. When the phase velocity ω_p/q of the plasmon wave exceeds the Fermi velocity of the material, energy can be transferred to individual electrons and the plasmon mode becomes highly damped; the effective oscillator strength df/dE falls rapidly to zero when θ exceeds θ_c. For $\beta > \theta_c$, β should therefore be replaced by θ_c in equation (14), giving a *total* MFP appropriate to large collection angles.

The plasmon total MFP exhibits a cyclic dependence on the atomic number Z due to the cyclic nature of the number z of quasi-free electrons per atom. This behaviour was recently confirmed by experiment and the free-electron formula found to give a MFP within a few per cent of the experimental values (Iakoubovskii *et al* 2008a, 2008b).

3.4. Surface plasmons and radiation loss

Even before a beam electron enters the specimen, its electric charge polarizes the entrance surface. In the case of a

conductor, this sets up a longitudinal charge-density wave $\cos(qx-\omega t)$ whose angular frequency of oscillation ω satisfies a boundary condition at the surface:

$$\varepsilon_a(\omega) + \varepsilon_b(\omega) = 0, \tag{15}$$

where $\varepsilon_b(\omega)$ and $\varepsilon_a(\omega)$ are relative permittivities of the specimen and its surroundings. The simplest case is an interface between vacuum and a free-electron metal: $\varepsilon_a(\omega) = 1$ and $\varepsilon_b(\omega) = 1 - \omega_p^2/\omega^2$. Equation (15) then gives $\omega = \omega_s = \omega_p/\sqrt{2}$, indicating that the energy-loss spectrum will include a surface-plasmon peak centred about an energy E_s given by

$$E_s = (h/2\pi)(\omega_p/\sqrt{2}) = E_p/\sqrt{2}. \tag{16}$$

For an insulator/metal boundary, where the permittivity of the insulator has a positive real part ε_1 and both insulator and metal have negligible imaginary parts at frequencies close to ω_s, equation (15) gives

$$E_s = E_p/(1+\varepsilon_1)^{1/2}. \tag{17}$$

In agreement with experiment (Powell and Swan 1960), Stern and Ferrell (1960) showed that equation (17) applies to an oxidized metal surface provided the oxide layer is thicker than about 3 nm. They also derived an expression for the probability of scattering (per unit solid angle Ω) of the incident electron as a result of surface-plasmon excitation:

$$\mathrm{d}P_s/\mathrm{d}\Omega = h[\pi^2 a_0 m_0 v(1+\varepsilon_1)]^{-1}\theta\theta_E(\theta^2+\theta_E^2)^{-2} f(\theta,\theta_i,\psi), \tag{18}$$

where $\theta_E = E/(\gamma m_0 v^2) = E/(2\gamma T)$ as previously; θ_i is the angle between the surface normal and the incident beam; ψ is the angle between the plane of incidence and the detector and $f(\theta,\theta_i,\psi) = [(1+\theta_E^2/\theta^2)/\cos^2(\theta_i) - (\tan\theta_i\cos\psi + \theta_E/\theta)^2]^{1/2} \approx 1$ for $\theta_i < 0.1$ rad, $\theta \gg \theta_E$.

For $\theta_i = 0$ (normal incidence), $f(\theta,\theta_i,\psi) = 1$ and the scattered-electron intensity is zero at $\theta = 0$, rising to a maximum at $\theta = \theta_E/\sqrt{3}$ and then falling proportional to θ^{-3} for $\theta \gg \theta_E$. Since θ_E is very small (<0.1 mrad typically), the surface-plasmon intensity is concentrated into even smaller angles than volume-plasmon scattering, which falls as θ^{-2} for $\theta \gg \theta_E$. Surface-mode contributions to the loss spectrum can therefore be minimized by displacing the angle-selecting aperture away from optic axis or by using a collection aperture with a central stop.

Alternatively, if an axial and relatively large collection aperture is used ($\beta \gg \theta_E$), the probability of surface-plasmon excitation at a single interface, for normal incidence ($\theta_i = 0$) and integrated around the E_s peak, is (Ritchie 1957, Stern and Ferrell 1960)

$$P_s = h[2a_0 m_0 v(1+\varepsilon_1)]^{-1}, \tag{19}$$

which is of the order of 1% at each surface for 100 keV incident electrons. This means that surface-plasmon peaks are prominent (relative to bulk-plasmon peaks) only for rather thin specimens ($t < 20$ nm). There is also a negative contribution ($-P_s/2$) around the bulk-plasmon energy E_p, arising from the so-called *begrenzungs* effect (Ritchie 1957).

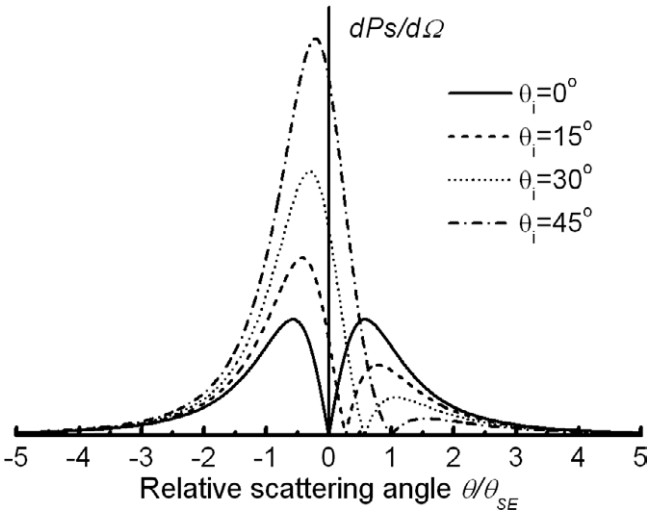

Figure 9. Angular distribution of surface-plasmon scattering within the plane of incidence, for electron beams with various angles of incidence θ_i relative to the surface-normal.

As the specimen is tilted away from perpendicular incidence, the angular distribution of surface-plasmon scattering becomes asymmetrical relative to the optic axis (see figure 9) and the integrated intensity increases by a factor $\approx 1/\cos\theta_i$. For large θ_i, surface-plasmon scattering dominates over bulk-plasmon peaks, as in the case of surface-reflection spectra where electrons are elastically reflected back into vacuum after penetrating only a short distance into the specimen (Powell 1968). A similar situation exists when the electrons are focused into a fine probe (sub-nanometre diameter) positioned within a few nanometres beyond the edge of a particle. In this *aloof mode* of spectroscopy, energy losses due to surface plasmons predominate (Howie 1983, Batson 2008).

To predict the energy dependence of surface-loss intensity, we must know the *energy dependence* of the permittivities on both sides of the interface. For perpendicular incidence, the interface-loss probability integrated up to an angle β is

$$\mathrm{d}P_s/\mathrm{d}E = (\pi a_0 k_0 T)^{-1}[(1/\theta_E)\tan^{-1}(\beta/\theta_E)] \times\{\mathrm{Im}[-4/(\varepsilon_a+\varepsilon_b)] - \mathrm{Im}[-1/\varepsilon_a] - \mathrm{Im}[-1/\varepsilon_b]\}. \tag{20}$$

This expression is symmetric with respect to the two media; the direction of travel of the electron does not matter. Negative terms of the form $\mathrm{Im}(-1/\varepsilon)$ indicate that the interface plasmon intensity occurs at the expense of volume-plasmon intensity (the energy-integrated oscillator strength being unaltered by the interface). This is the *begrenzungs* effect, which arises because the bulk-plasmon wake requires a distance $\lambda_p/4 = (\pi/2)(v/\omega_p)$ to become established on each side of the interface (Garcia de Abajo and Echenique 1992, Egerton 1996).

Our previous equations all assume that the thickness t of each material is large enough that there is negligible electrostatic coupling between the surface-plasmon fields at its two surfaces: $q_s t \gg 1$, where $q_s = k_0\theta$ for perpendicular incidence. Kröger (1968) gave a more complete derivation of the energy-loss intensity for an electron transmitted through a

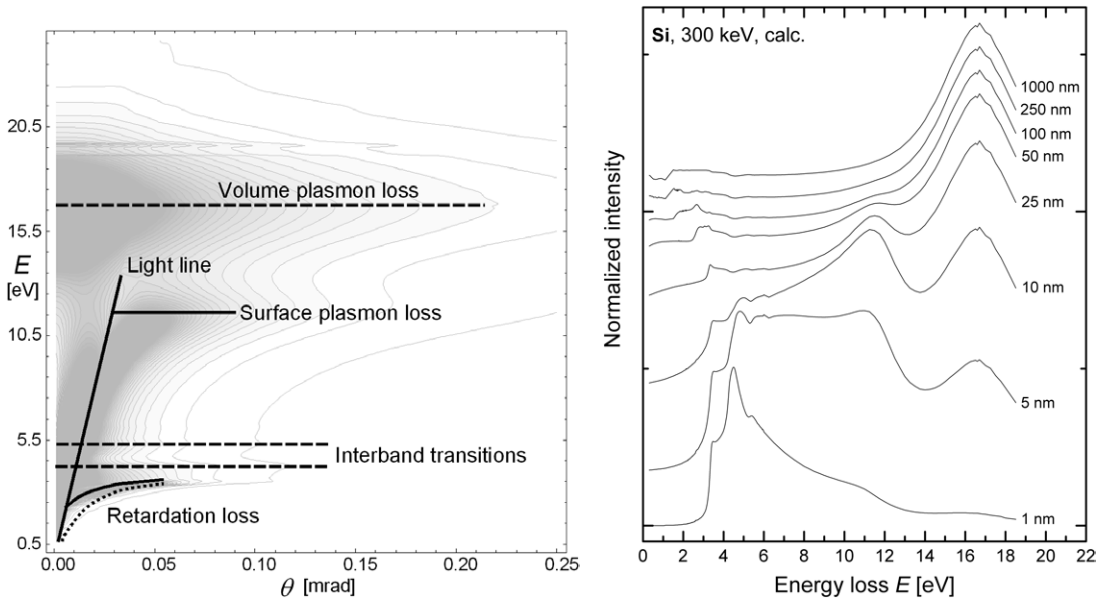

Figure 10. (*a*) Schematic and contour plot (grey background) showing the calculated energy-loss and angular dependence of intensity for a 50 nm Si specimen with 300 keV incident electrons. (*b*) Calculated energy-loss spectra for 2.1 mrad collection semiangle, 300 keV incident electrons and various thicknesses of Si, assuming no surface-oxide layer. Reproduced from Erni and Browning (2008), copyright Elsevier.

foil of any thickness, including coupling of the plasmon modes between the two surfaces and a relativistic retardation effect related to the generation of Čerenkov radiation. His formula for the energy-loss intensity contains seven terms, of which the last three vanish for normal incidence ($\theta_i = 0$). The first term is proportional to specimen thickness and corresponds to bulk losses; other terms represent surface excitations. Several of the terms contain a resonance denominator that becomes zero at a certain energy loss E, corresponding to emission of Čerenkov radiation when the electron speed v is higher than the speed of light: $c/\varepsilon_1(E)^{1/2}$ in the specimen. This radiation loss gives rise to peaks (at a few electron volts loss) that can interfere with bandgap measurements in semiconductors (Stöger-Pollach *et al* 2006). In the TEM, the Čerenkov and surface-plasmon contributions can be minimized by using an off-axis collection aperture or an on-axis aperture with a central stop (Stöger–Pollach 2008). However, these steps are only effective for near-parallel illumination; a highly-focused STEM probe involves incident convergence angles of several millirads.

Erni and Browning (2008) have evaluated the Kröger equations for several semiconductors and an insulator (Si_3N_4); see figure 10. Volume retardation leads to a peak in the energy-loss spectrum below 10 eV and a peak in the angular distribution below 0.1 mrad, but when the specimen is thinner than about 300 nm, surface-mode scattering becomes important and results in guided-light modes arising from total internal reflection of the Čerenkov radiation. Above 100 nm thickness, the low-loss spectra are dominated by the volume plasmon and Čerenkov peaks, around 10 nm by volume and surface plasmons and at very low thickness by surface and guided-light modes. The guided modes have a dispersion lying between the light line for vacuum ($\omega = cq$) and that in the semiconductor ($\omega = cq/n = cq/\varepsilon_1^{1/2}$), as explained by Raether (1980).

Both Čerenkov and surface-plasmon modes complicate the Kramers–Kronig process of obtaining dielectric data from EELS measurements. Čerenkov effects are particularly severe in the case of insulators such as diamond (Zhang *et al* 2008). New Čerenkov modes have been predicted for electrons passing close to small particles (Itskovsky *et al* 2008) and new surface-plasmon modes in small particles have been revealed by energy-filtered imaging (Nehayah *et al* 2007). This is an active area of research, made possible by recent improvements in energy resolution.

3.5. Single-electron excitation and fine structure

In addition to the collective response, a transmitted electron can excite individual atomic electrons to quantum states of higher energy. Evidence for these single-electron excitations is seen in the form of fine-structure peaks that occur at energies above or below the plasmon peak or that modulate its otherwise smooth profile. If a strong single-electron peak occurs at energy E_i, the plasmon peak is displaced in energy in a direction away from E_i, in accordance with coupled-oscillator theory (Raether 1980).

Single-electron transitions are readily observed in the energy-loss spectra of transition metals, where d-electrons contribute multiple peaks, in organic compounds and in hydrated biological specimens, partly due to the water content (Sun *et al* 1993). Polymers show some fine structure (and a 7 eV peak if double bonds are present) together with a broad peak in the range 20–25 eV, showing plasmon-like dispersion, which can be interpreted as a plasmon resonance (Barbarez *et al* 1977).

The angular distribution of the single-electron intensity is the same as for volume plasmons but there is a more gradual falloff from the Lorentzian formula at higher angles. Dispersion (change in peak energy with angle) should be

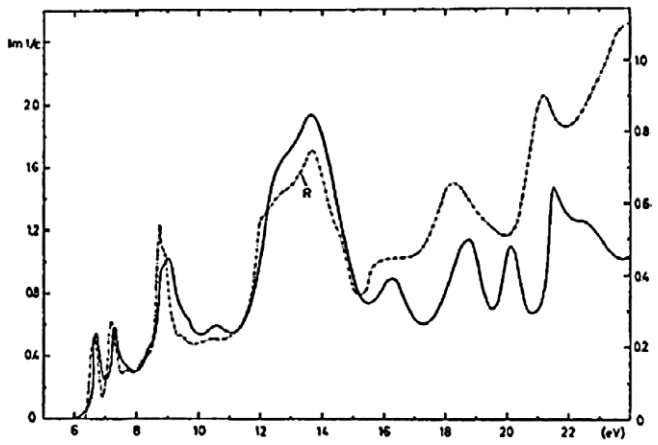

Figure 11. Energy-loss function of KBr from energy-loss measurements (Keil 1968; full line) compared with optical data (dashed line). Peaks below 10 eV are due to exciton states; the 13–14 eV peak may be a plasmon resonance. Reproduced from Raether (1980) with kind permission of Springer Science and Business Media.

negligible, which is sometimes used to determine if a peak arises from collective or single-electron excitation.

In a non-metal, the low-loss fine structure represents interband transitions that can be calculated with the aid of density-functional theory (Keast 2005). The spectral intensity is related to the joint density of states between conduction and valence bands. Ideally the inelastic intensity should remain zero up to an energy loss equal to the bandgap energy. However, exciton peaks can occur due to transitions to exciton states below the conduction band, as in the case of alkali halides; see figure 11.

3.6. Core-electron excitation

The atomic electrons that are located in inner shells (labelled K, L etc from the nucleus outwards) have binding energies that are mostly hundreds or thousands of electron volts. Their excitation by a transmitted electron gives rise to *ionization edges* in the energy-loss spectrum, the equivalent of absorption edges in XAS. Since core-electron binding energies differ for each element and each type of shell, the ionization edges can be used to identify which elements are present in the specimen. They occur superimposed on a background that represents energy loss due to valence electrons (for example, the high-energy tail of a plasmon peak) or ionization edges of lower binding energy. This background contribution can be extrapolated and removed for quantitative elemental or structural analysis.

In a solid specimen, inner-shell excitation implies transitions of the core electrons to empty states above the Fermi level. Because of the strong binding of these electrons to the nucleus, collective effects are less important than for valence-electron excitation, allowing the basic shapes and properties of the edges to be approximated by single-atom theory. As we saw in equation (5), a key quantity in the atomic theory of inelastic scattering is $\mathrm{d}f/\mathrm{d}E$, known as the generalized oscillator strength (GOS) since it is in general a function of transferred momentum q (related to the electron scattering

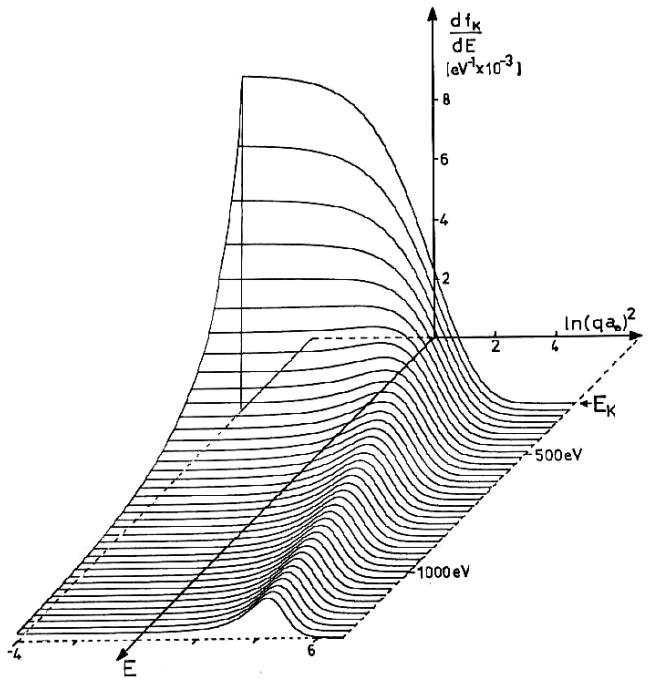

Figure 12. Bethe surface for K-shell ionization of a carbon atom, based on a hydrogenic model (Egerton 1979). The oscillator strength is zero for energy loss below the ionization threshold E_K.

angle θ) as well as transferred energy E (Inokuti 1971). For the hydrogen atom (Coulombic wavefunctions), $\mathrm{d}f/\mathrm{d}E$ is given by an analytical formula and this can be adapted to other atoms by suitable scaling. A plot of the hydrogenic GOS for K-shell ionization of a carbon atom as a function of q and E, the *Bethe surface*, is shown in figure 12.

The E-dependence at the left-hand boundary of figure 12 indicates that this ionization edge has a sawtooth shape: a rapid rise at the ionization threshold followed by a monotonic decay, typical of K-edges. This decaying $\mathrm{d}f/\mathrm{d}E$ leads to a core-loss differential cross section:

$$\mathrm{d}^2\sigma_\mathrm{c}/\mathrm{d}\Omega\,\mathrm{d}E = (4a_0^2R^2/T)(1/E)[\mathrm{d}f(q,E)/\mathrm{d}E] \times(\theta^2+\theta_\mathrm{E}^2)^{-1}, \tag{21}$$

and a corresponding core-loss intensity that resembles an inverse power law: BE^{-s}. Just above the ionization threshold E_K (and $qa_0 < 1$), the GOS approximates to its q-independent optical value $\mathrm{d}f(0,E)/\mathrm{d}E$ and equation (21) predicts a Lorentzian angular dependence. This *dipole region* corresponds to scattering with a relatively large impact parameter from strongly-bound core electrons. Integrating up to a scattering angle β gives

$$\mathrm{d}\sigma_\mathrm{c}/\mathrm{d}E \approx (4\pi a_0^2R^2/T)(1/E)[\mathrm{d}f(0,E)/\mathrm{d}E]\ln(1+\beta^2/\theta_\mathrm{E}^2). \tag{22}$$

For $E \gg E_\mathrm{K}$, the oscillator strength becomes concentrated around a non-zero q, given by $(qa_0)^2 \approx E/R$, which forms a *Bethe ridge* on the GOS plot; see figure 12. This situation approximates to close-collision Rutherford scattering from a free and stationary electron, for which momentum and energy conservation would lead to a single scattering angle, uniquely related to energy loss: $\theta \approx (E/E_0)^{1/2}$.

Other atomic shells (L, M, etc) have corresponding Bethe surfaces but are split into several components with different bonding energies. The L-edge has three components; the L_1 edge (2s excitation) has the hydrogenic sawtooth shape but is relatively weak (especially for small collection angle β) since it violates the dipole sum rule ($\Delta l = \pm 1$). L_2 and L_3 edges (excitation of $2p^{1/2}$ and $2p^{3/2}$ electrons) satisfy the sum rule but many of them have a rounded profile because the effective potential (for angular quantum number $l = 1$) is delayed by a centrifugal-barrier term (Inokuti 1971, Inokuti *et al* 1978). For lower-Z elements, the thresholds are so close in energy that the two edges overlap and are described as L_{23}.

Other L-edges have sharp peaks at the threshold, known as *white lines*, because they appeared as white areas when an x-ray absorption spectrum was recorded as a photographic negative. Examples include the L_2 and L_3 edges of transition metals and their compounds, where the white lines can be attributed to a high density of empty d-states just above the Fermi level. M-edges are similar; M_4 and M_5 edges (3d excitation) are rounded (with delayed maxima) in metals such as Nb, Mo and Ag but show sharp white-line peaks in rare-earth metals (e.g. La) due to a high density of final f-states. An atlas showing the edge shapes for most chemical elements is available in print form (Ahn and Krivanek 1983) and on CD (Ahn 2004).

Unless recorded from specimens that are very thin ($t/L \ll 1$, where L is the plasmon MFP), an ionization edge is broadened in energy as a result of plural scattering. Here plural scattering means the excitation of one or more plasmons or interband transitions by the same transmitted electron that generated the core excitation. Plural scattering causes the thin-specimen edge profile to be convolved with that of the low-loss spectrum, increasing the intensity at energies 10 eV or more beyond the threshold; see figure 13. If the low-loss spectrum has been measured, the plural scattering can be removed by a Fourier-ratio deconvolution (Egerton and Whelan 1974). In principle, this procedure also allows spectra to be 'sharpened' (enhanced in energy resolution) but the noise content is then amplified. Bayesian techniques (maximum-entropy or maximum-likelihood deconvolution) have been explored as a way of dealing more effectively with this noise problem (Overwijk and Reefman 2000, Kimoto *et al* 2003, Gloter *et al* 2003, Lazar *et al* 2006, Egerton *et al* 2006a).

3.7. Core-loss fine structure

White-line peaks are just one example of fine structure in an ionization edge. In general, the core-loss intensity $J_c(E)$ (i.e. spectral intensity minus pre-edge background) is given by an expression known as the Fermi golden rule:

$$J_c(E) \propto d\sigma_c/dE \propto M(E)^2 N(E) \propto (df/dE)N(E). \qquad (23)$$

Here $M(E)$ represents an atomic matrix element, closely related to the atomic oscillator strength df/dE, while $N(E)$ is the density of final states in the electron transition. As indicated in equation (23), solid-state effects modulate the basic shape of the edge derived from atomic theory. Core-loss EELS therefore provides a measure of the energy dependence of the density of empty states in the conduction band, similar to

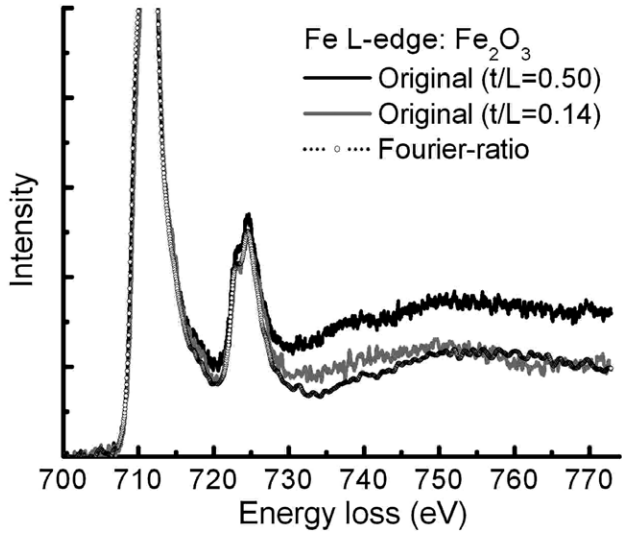

Figure 13. Background-subtracted Fe L-edge (showing L_3 and L_2 white lines at 712 and 724 eV) recorded from thick and thin specimens, and after removal of plural scattering by Fourier-ratio deconvolution.

XAS and complementary to an x-ray photoelectron spectrum (XPS), which reflects the density of *filled* valence-band states.

The density of states determined by electrical measurements differs from $N(E)$, which is a *local* density of states (LDOS) evaluated at the excited atom. As a result, $N(E)$ varies at different crystallographic sites, leading to dissimilar fine structure in the corresponding ionization edges. Further, $N(E)$ is a *symmetry-projected* density of states, governed by the dipole selection rule. The excitation of K-shell (1s) electrons reveals the density of empty 2p states, whereas L_2 or L_3 (2p) excitation uncovers 3d and (to a lesser extent) 3s states.

In principle, equation (23) involves a *joint* density of the initial and final states involved in the transition or a convolution of the appropriate densities of states. However, the core-level initial state is relatively sharp in energy, a delta function in the first approximation. To a better approximation, it is represented by a Lorentzian function whose natural width ranges from a fraction of an electron volt (for light elements) to several electron volts for heavier elements (Krause and Oliver 1979). This *initial-state* broadening arises from the short life of the core hole, which is rapidly filled, leading to x-ray or Auger emission. *Final-state* broadening reflects the lifetime of the excited core electron and depends on its kinetic energy (i.e. energy loss above threshold). Since the core hole increases the charge at the centre of the atom by one unit, its effect is often simulated (in fine-structure calculations) by using a potential that corresponds to the next-higher element in the periodic table, the so-called $Z + 1$ approximation.

There are two basic methods of calculating ionization-edge fine structure. The first of these involves a reciprocal-space calculation of band structure and LDOS. For example, the full-potential linearized augmented plane wave (FLAPW) method can be implemented by using the Wien2k computer program (Hébert 2007). The second procedure is a real-space calculation, originally used for simulation of an extended x-ray absorption fine structure (EXAFS). This structure arises from

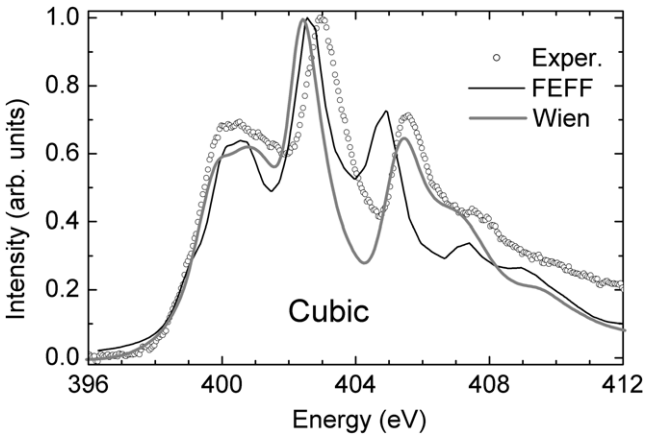

Figure 14. Nitrogen K-loss spectrum of cubic GaN, as recorded by a monochromated TEM-EELS system and as calculated by real-space (FEFF) and band-structure (Wien2k) methods. Reprinted with permission from Moreno *et al* (2006), copyright American Institute of Physics.

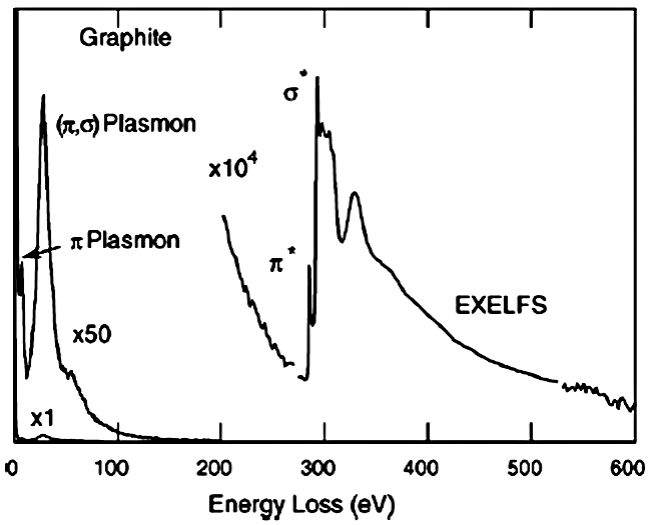

Figure 15. Energy-loss spectrum of graphite, recorded with a small-diameter probe and large collection angle. The K-edge shows peaks due to transitions of 1s electrons to π^* and σ^* antibonding state. Reproduced from Batson (2008), copyright Elsevier.

interference between the excited-electron wave, wavevector $k = (2\pi/h)[2m(E - E_c)]^{1/2}$, with waves backscattered from each shell (index j, radius R_j) of the surrounding atoms, whose backscattering amplitude is $f_j(k)$. In the single-scattering approximation of Sayers *et al* (1971), the normalised fine-structure intensity is

$$\chi(k) = \Sigma_j [N_j/(kR_j^2)] f_j(k) \sin(2kR_j + 2\delta_c + \phi) \times [\exp(-2R_j/\lambda_a(k)] \exp(-2\sigma^2 k^2). \quad (24)$$

$2kR_j$ represents the phase difference due to the return path length $2R_j$ while $2\delta_c$ and ϕ are phase shifts due to the central and backscattering atoms. The exponential terms represent attenuation of the ejected-electron wave by inelastic scattering and phonon excitation. Equation (24) successfully predicts EXAFS or extended energy-loss fine structure (EXELFS) but in the near-edge region (within 50 eV of the threshold) multiple scattering becomes important and must be included in the theory (Moreno *et al* 2007). The calculation is then referred to as a multiple-scattering (MS or RSMS) calculation. Real-space calculations are particularly useful for aperiodic systems (e.g. isolated molecules) where the band-structure approach can be cumbersome (although possible by analysing a hypothetical crystal of repeating molecules). Equation (24) can be evaluated for different numbers of atomic shells (range of j) and this procedure is usually carried out to ensure that the chosen range of j is large enough for convergence. Calculations on various materials indicate that the volume of specimen giving rise to the fine structure has a diameter of the order of 1 nm, centred on the excited atom (Wang *et al* 2008a).

Although both methods of calculation are still being refined, there is now reasonable agreement between the predictions of real-space and reciprocal-space calculations and improved correlation with experimental data; see figure 14.

3.8. Chemical shifts

In x-ray photoelectron spectroscopy (XPS), where electrons are excited from atomic core levels of a solid into the adjacent vaccum, a chemical shift of the associated spectral peak represents a change in core-level energy arising from the change in the effective charge on the atom. In EELS, changes in the chemical environment of an atom can cause a similar shift in the threshold energy of an ionization edge, up to a few electron volts. But at the edge threshold, the final state of the core electron lies just above the Fermi level and below the vacuum level, so in this case any chemical shift includes not only the effect of electron transfer to the atom but also change in valence-band width, due to redistribution of the coordinates of neighbouring atoms. This second factor is predominant in the case of metals and it implies that, while the core-loss fine structure reflects the density of unoccupied states above the Fermi level, the chemical shift carries information about the *occupied* states (Muller 1999). The ionization threshold of a metal generally increases upon oxidation and this positive chemical shift can be attributed to the formation of an energy gap which elevates the empty conduction-band states to higher energy.

3.9. Core-loss spectroscopy of anisotropic materials

While the energy-loss spectrum of a cubic crystal is independent of its orientation relative to the electron beam, this is not true for an anisotropic crystal. A good example is graphite, a uniaxial hexagonal material with σ hybridized wavefunctions providing strong interatomic bonding within basal planes and π orbitals directed perpendicular to these planes. The K-loss spectrum represents transitions from 1s states to empty π^* and σ^* antibonding orbitals lying above the Fermi level. The π^* component gives rise to a sharp peak at 285.4 eV, the σ component to a broad peak centred around 292.5 eV; see figure 15.

Leapman *et al* (1983) give expressions for the angular dependence of these two components (within the tilt plane) when the specimen is oriented so that the z-axis (perpendicular

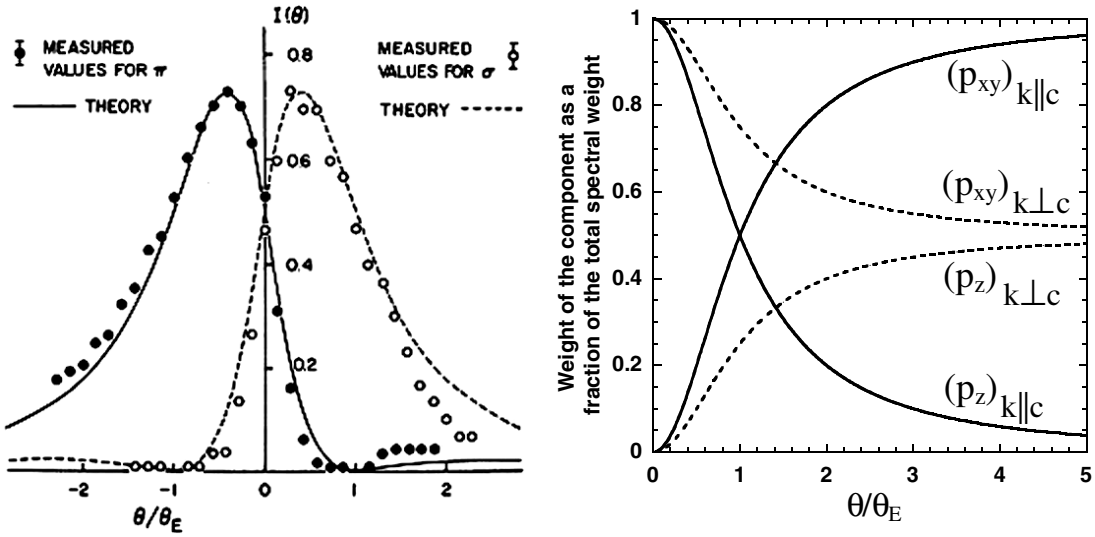

Figure 16. (*a*) Calculated and measured angular distributions of π and σ intensity in the K-loss spectrum of graphite, within the plane of tilt and for the specimen oriented with a tilt angle $\gamma = -45^\circ$ (Leapman *et al* 1983). (*b*) Axial (z) and basal-plane (xy) intensities as a function of the collection angle (Klie *et al* 2003). Reprinted with permission, copyright American Institute of Physics.

to the basal plane) makes an angle γ relative to the incident beam:

$$J(\pi) \propto \cos^2(\alpha - \gamma)/(\theta^2 + \theta_E^2), \tag{25}$$

$$J(\sigma) \propto \sin^2(\alpha - \gamma)/(\theta^2 + \theta_E^2). \tag{26}$$

Here $\alpha \approx \tan^{-1}(\theta/\theta_E)$ is the angle between the direction of momentum transfer and the incident-beam direction. For $\gamma = 0$, $J(\pi) \propto \theta_E^2/(\theta^2+\theta_E^2)^2$ and $J(\sigma) \propto \theta^2/(\theta^2+\theta_E^2)^2$, so the π-intensity has a narrow forward-peaked angular distribution, falling by a factor of 4 between $\theta = 0$ and $\theta = \theta_E$. Conversely, the σ intensity is zero at $\theta = 0$ and rises to a maximum at $\theta \approx \pm\theta_E$; the sum of these two components is Lorentzian. Tilting the specimen makes these angular distributions asymmetric (qualitatively similar to the surface-plasmon case, figure 9) and allows the two components to be measured separately. Tilting to 45° is advantageous because it maximizes the separation between the two angular distributions and makes their relative intensities similar; see figure 16(*a*).

For a uniaxial crystal (MgB_2), Klie *et al* (2003) have integrated the z-axis and basal-plane (xy) intensities over all azimuthal angles and up to a scattering angle β. For an electron beam parallel to the c-axis, these integrated intensities are equal when $\beta = \theta_E$ (solid curves in figure 16(*b*)).

To act as a reference when analysing anisotropic crystals, it is useful to have a core-loss spectrum that is independent of orientation. This can be achieved by using a spectrometer entrance aperture that admits scattering up a particular angle θ_m, known as the *magic angle*. Nonrelativistic theory gives $\theta_m \approx 4\theta_E$ but this relation was shown to be inaccurate following the development of fully relativistic equations of core-loss scattering (Jouffrey *et al* 2004, Schattschneider *et al* 2005, Sun and Yuan 2005), an extension of earlier theory due to Møller (1932). The relativistic retardation effect results in a force perpendicular to the scattering vector $\boldsymbol{q}$ and this transverse excitation introduces additional terms in the expression for scattered intensity. Fano (1956) added the transverse and longitudinal effects incoherently, permissible for an isotropic specimen, but for an anisotropic crystal there is an interference term that cannot be neglected.

The magic-angle condition provides a spectrum identical to that recorded from a random-polycrystalline (orientation-averaged) isotropic material and in this condition the π and σ interference terms exactly cancel. This occurs at $\theta_m = F\theta_E$ where $F \approx 4$ in the nonrelativistic limit, falling to 2.25 for $E_0 = 100$ keV and 1.46 for $E_0 = 200$ keV (Schattschneider *et al* 2005). Implications of these relativistic effects for the analysis of fine structure are being evaluated (Hebert *et al* 2006, Hu *et al* 2007). Recently Sorini *et al* (2008) have suggested that dielectric effects may increase F for energy losses below 100 eV.

4. Applications and limitations of TEM-EELS

As discussed in the introduction, EELS is one of several techniques for materials analysis in the TEM and is usually employed in conjunction with electron diffraction and imaging.

4.1. Thickness measurement

It is often useful to know the local thickness of a TEM specimen, for example, to obtain defect or elemental concentrations from a TEM image or energy-loss spectrum. Among several *in situ* methods for thickness measurement, EELS provides a technique that is general (applicable to crystalline and amorphous samples) and relatively rapid (it involves recording the low-loss spectrum, where the intensity is relatively high).

The most common procedure is the *log-ratio method*, based on the measurement of the integrated intensity I_0 of a zero-loss peak relative to the integral I_t of the whole spectrum. Poisson statistics of inelastic scattering, equation (9), leads to the formula

$$t/L = \log_e(I_t/I_0), \tag{27}$$

where L is a plasmon or total-inelastic MFP. To capture most of the intensity, I_t need only be integrated up to about 200 eV, assuming a typically thin TEM specimen ($t < 200$ nm). If necessary, the spectrum can be extrapolated until the spectral intensity becomes negligible. Equation (27) can be rapidly implemented at each pixel of a spectrum image, yielding a semi-quantitative thickness map.

The ratio t/L provides a measure of the *relative* thickness of different areas of a specimen (if it has a uniform composition); knowing the absolute thickness t requires a value of the inelastic MFP for the incident-electron energy E_0 and collection angle β used to record the data. If no angle-limiting TEM aperture is used, lens bores limit β to a value in the range 100–200 mrad, large enough to make L a *total* MFP, which is tabulated for common materials at electron energies of 100 and 200 keV (Egerton 1996, Iakoubovskii *et al* 2008a, 2008b). This MFP is also appropriate when a large TEM objective aperture is used (e.g. $\beta \approx 30$ mrad), although a correction for incident-probe convergence (semiangle α) may then be necessary (Iakoubovskii *et al* 2008a, 2008b).

If the collection angle is small enough to correspond to the dipole region of scattering, a β-dependent MFP can be estimated from equation (14), with E_p taken as the energy of the main peak in the low-loss spectrum. If the mean atomic number of the specimen is known, other empirical procedures are available for calculating $L(E_0, \beta)$ (Egerton 1996). The accuracy of the log-ratio method depends largely on how well the MFP is known, which varies from one material to another, but as a rough guide, thickness can probably be measured to about 20% accuracy in most cases.

A potentially more accurate thickness measurement applies a Kramers–Kronig sum rule to the low-loss spectrum $J(E)$:

$$t = (4a_0 T/I_0)[1 - \mathrm{Re}(1/\varepsilon)]^{-1} \times \int J(E)E^{-1}[\ln(1 + \beta^2/\theta_E^2)]^{-1}\mathrm{d}E. \quad (28)$$

The integral is over all energy losses, excluding the zero-loss peak and can be evaluated by running a short computer script, given as a menu item in the Gatan software that is commonly used to acquire and process EELS data. As equation (28) is based on dipole theory, the spectrum should be collected with a small value of β and α (both less than 10 mrad). The $1/E$ weighting in equation (28) implies that the spectrum need only be recorded up to an energy loss of around 100 eV but that the energy resolution must be sufficient to allow the spectral intensity to fall close to zero after the zero-loss peak, so that any tail of that peak can be excluded from the integral. A potential disadvantage is the need to know $\mathrm{Re}(1/\varepsilon)$ at $E \approx 1$ eV. However this quantity can be taken as zero for a metal or semi-metal and as $1/n^2$ for a semiconductor or insulator whose refractive index is n in the visible region. Therefore the method actually requires less information about the specimen composition than the log-ratio method. Equation (28) assumes that Fourier-log deconvolution has been used to remove plural scattering from $J(E)$, although this step can be avoided if the specimen is thinner than 100 nm and empirical corrections are applied for plural scattering and surface-plasmon excitation (Egerton 1996).

The Bethe or f-sum rule $\int (\mathrm{d}f/\mathrm{d}E)\mathrm{d}E = Z$ provides a measurement a local *mass thickness*, based on

$$\rho t = uT(4\pi a_0^2)R^2 I_0(A/Z) \int EJ(E)[\ln(1 + \beta^2/\theta_E^2)]^{-1}\,\mathrm{d}E, \quad (29)$$

where $u = 1.67 \times 10^{-27}$ kg is the atomic mass unit. Because of the E-weighting in equation (29), energy resolution is unimportant but plural scattering and any instrumental background must be properly removed, since the spectrum needs to be integrated up to a high energy loss (Crozier and Egerton 1989). Alternatively a 'partial sum rule' can be assumed, integrating up to an energy just below the ionization threshold of a particular inner shell and replacing the atomic number Z by the number of electrons per atom in all shells of lower binding energy, including conduction or valence electrons. In the case of carbon, this means integrating up to about 280 eV and taking $Z = 4$ (but $A = 12$) in equation (29). A significant advantage of equation (29) is that it is relatively insensitive to the chemical composition of the specimen; for light-element materials (including organic compounds and biological tissue), A/Z can be taken as approximately 2 if the spectrum is measured and integrated up to about 1000 eV (Crozier and Egerton 1989). Little used up to now, this method probably deserves more attention.

4.2. Electronic properties of semiconductors and insulators

As the size of silicon devices shrinks towards nanometre dimensions, TEM and EELS are used increasingly to study device properties. For example, it is useful to know how the bandgap of a semiconductor or a dielectric changes within a device. The TEM provides the necessary spatial resolution but since these bandgaps are at most a few electron volts, energy resolution is also vital and a monochromated system (FWHM ≈0.2 eV) is almost essential. Monochromated TEM-EELS allowed Browning *et al* (2007)) to measure the increase in bandgap with decreasing particle size of CdSe quantum dots; see figure 17.

One technical problem is the overwhelming intensity of the zero-loss peak, whose ($E > 0$) tail extends to several times the FWHM. Stoeger-Pollach (2008) compared four methods of removing this tail and recommended a procedure involving Fourier-ratio deconvolution rather than subtraction methods. To minimize an additional tail due to the point-spread function of the electron detector, the spectrum is recorded with high dispersion (e.g. 0.05 eV/channel). Problems also arise from surface-plasmon and retardation (Cerenkov) modes, which add peaks below 10 eV. These latter contributions can be minimized by using an off-axis detector or by subtracting the spectra recorded with small and large collection angles (Stoeger-Pollach 2008), equivalent to a collection aperture with a central stop.

Rafferty and Brown (1998) pointed out that the low-loss fine structure involves a joint density of states multiplied by a matrix element that differs in the case of direct and indirect transitions. Assuming no excitonic states, their analysis showed that the onset of energy-loss intensity at the bandgap

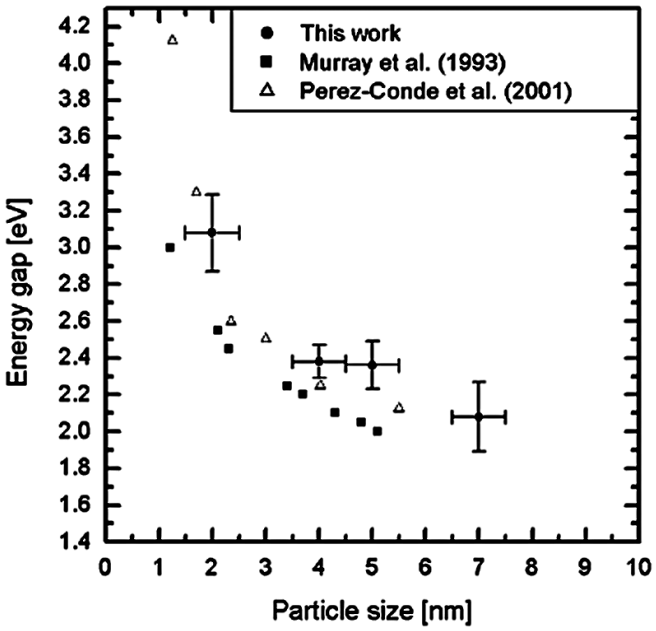

Figure 17. Bandgaps measured by EELS (with error bars) compared with those from optical measurements (square data points) and theoretical studies (triangles). From Browning *et al* (2007), by permission of Cambridge University Press.

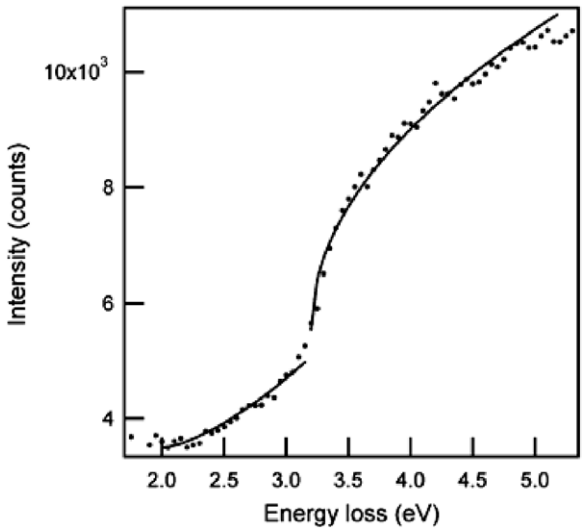

Figure 18. Inelastic intensity recorded from cubic GaN using a monochromated TEM-EELS system. Above the bandgap energy ($E_g = 3.1$ eV), data are fitted to the direct-gap expression $(E - E_g)^{0.5}$, at lower energy to the indirect-gap expression $(E - E_g)^{1.5}$ where $E_g = 2$ eV. Reproduced from Lazar *et al* (2003), copyright Elsevier.

energy E_g is proportional to $(E - E_g)^{1/2}$ for a direct gap and $(E - E_g)^{3/2}$ for an indirect gap.

Cubic GaN is a direct-gap material whose inelastic intensity (after subtracting the zero-loss tail) fits well to $(E - E_g)^{1/2}$ for $E > E_g$ (Lazar *et al* 2003). For $E > E_g$, there is some residual intensity that may be evidence of indirect transitions in a surface-oxide layer, since it can be fitted to a $(E - E_g)^{3/2}$ function; see figure 18.

Figure 19 shows low-loss spectra recorded from the anatase phase of TiO_2 (indirect gap ≈3.05 eV) and from a related hydroxylated material $H_2Ti_3O_7$ in the form of 8 nm diameter multiwalled nanotubes. Below 5 eV, the spectra can be fitted to a $(E - E_g)^{1.5}$ function but in the case of the nanotube, some additional intensity below 4 eV may indicate transitions involving defect states introduced by the hydroxyl groups (Wang *et al* 2008b). Note that these fits were performed on the spectra recorded with an off-axis spectrometer entrance aperture ($q \sim 1\ \text{nm}^{-1}$), in order to minimize unwanted surface-plasmon and Cerenkov-loss contributions. Conversely, an electron probe focused a few nanometres *outside* a nanotube or small particle (aloof mode) generates mainly surface rather than bulk-mode excitations.

Crystalline defects greatly affect the electrical and mechanical properties of materials, often adversely. High-resolution TEM can reveal the atomic arrangement of individual defects while EELS gives information on their local electronic structure and bonding. Combining this information can lead to an understanding of how the atomic structure and physical properties are related. Using a high-resolution STEM, Batson *et al* (1986) could detect inelastic scattering due to localized states (within the 1.26 eV bandgap of GaAs) at a single misfit dislocation. Although strong diffraction in a crystalline specimen makes the interpretation of inelastic scattering more complicated, channelling directs the electrons down atomic columns (if the beam is aligned with a crystal axis) and improves the spatial resolution (Loane *et al* 1988). The high-resolution STEM uses an annular dark-field (ADF) detector that collects high-angle elastic scattering (proportional to Z^2) that provides good atomic-number contrast in a high-resolution ADF image. Given adequate probe stability, this image allows the electron beam to be positioned on an atomic column and held there long enough to enable useful spectra to be recorded (Duscher *et al* 1998).

4.3. Plasmon spectroscopy

The plasmon energy is related to mechanical properties of a material; large E_p implies a high valence-electron density, arising from short interatomic distances and/or a large number of valence electrons per atom, both of which lead to strong interatomic bonding. More specifically, the elastic, bulk and shear modulus all correlate with the square of the plasmon energy, although there is a fair amount of scatter; see figure 20. Oleshko and Howe (2007) have used this relation to deduce the mechanical properties of metal-alloy precipitates that are too small to be probed by nanoindentation techniques. Gilman (1999) showed that E_p is also correlated with surface energy, Fermi energy, polarizability (for metals) and band gap (for semiconductors). The implications have yet to be exploited.

Daniels *et al* (2003) used plasmon-loss mapping to investigate the mechanical properties of graphitic materials at a spatial resolution of 1.6 nm. By taking the *ratio* of intensities at 22 and 27 eV (either side of the $\sigma + \pi$-plasmon peak), they removed image contrast due to variations in specimen orientation and thickness. The plasmon energy itself was shown to be independent of specimen orientation but it increased after the specimen was annealed, indicating an increase in density and stronger bonding. Plasmon-loss

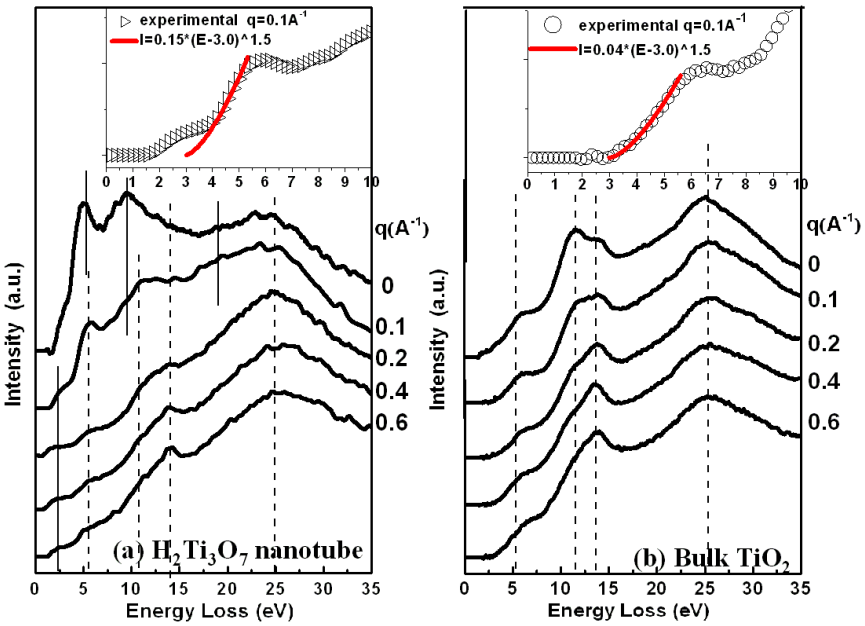

Figure 19. Low-loss spectra from (*a*) $H_2Ti_3O_7$ nanotube and (*b*) anatase TiO_2, recorded as a function of the magnitude q of the inelastic-scattering vector. Insets at top show fits of the inelastic intensities to a $(E - E_g)^{1.5}$ function. Reprinted with permission from Wang *et al* (2008b), copyright American Institute of Physics.

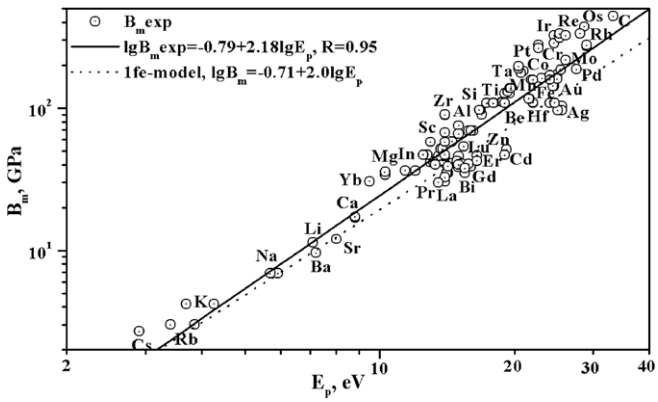

Figure 20. Bulk modulus plotted against plasmon energy for various elements. Reprinted with permission from Oleshko and Howe (2007), copyright American Institute of Physics.

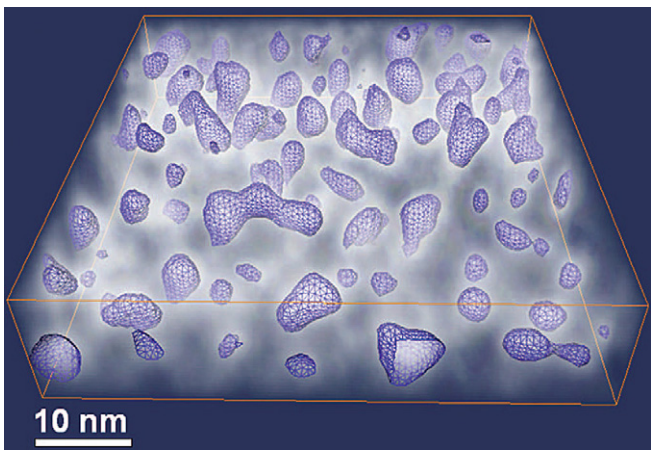

Figure 21. Tomographic reconstruction of silicon particles in silicon oxide. White 'fog' represents the plasmon-loss (17 eV) intensity; the silicon particles are rendered as mesh images at a constant intensity threshold. Reprinted with permission from Yurtsever *et al* (2006), copyright American Institute of Physics.

spectroscopy or mapping is attractive for examining radiation-sensitive materials because the intensity greatly exceeds the core-loss intensity, so recording times (for achieving adequate signal/noise ratio) and radiation dose are much lower.

Silicon nanoparticles could provide a light-emission system that would make optoelectronics compatible with silicon-processing technology. Yurtsever *et al* (2006) fabricated a dispersion of Si particles, by annealing silicon oxide films deposited by chemical-vapour deposition of silane. Cross-sectional (XTEM) samples showed little contrast, the MFPs for Si and SiO_2 being very similar. However the plasmon energies differ: 17 eV in Si but 23 eV in SiO_2, so energy-selective imaging gives a two-dimensional view of the nanoparticles. A more useful three-dimensional visualization was obtained with the aid of *electron tomography*, based on a series of TEM images recorded at many different specimen tilts (Gass *et al* 2006, Frank 2007); in this case, up to ±60° tilt in 4° increments. Computer software allowed alignment and reconstruction of the 17 ± 2 eV images in three dimensions; see figure 21. The particles themselves have soft outlines, probably reflecting the delocalization of plasmon scattering (∼2 nm, see later) but they were delineated by choosing a threshold intensity and representing the intensity contour as a mesh image. This technique made the particles more visible and showed that they have irregular shapes. Their complex morphology may explain the broad spectral range of photo- and electro-luminescence observed in this material, while the large surface area of each particle could account for the high efficiency of light emission.

French *et al* (1998) have used spectrum-imaging combined with Kramers–Kronig analysis to study dispersion

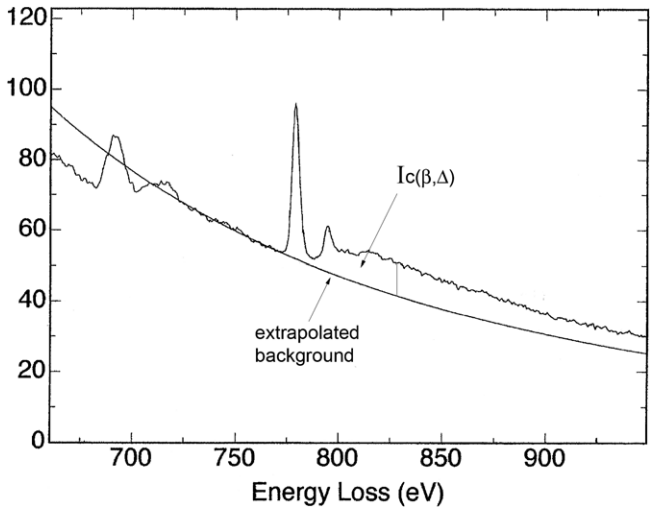

Figure 22. Procedure for elemental quantification, based on background extrapolation and integration of the intensity (above background) over a range Δ beyond the edge threshold.

(van der Waals) forces in silicon nitride. Characterized by Hamaker constants, these forces are important in determining intergranular strength in ceramic materials.

4.4. Elemental analysis

Because each ionization edge occurs at an energy loss that is characteristic of a particular element, EELS can be used to identify the elements present within the region of specimen defined by the electron beam. If the background to a particular edge can be extrapolated and subtracted, the remaining core-loss intensity provides a quantitative estimate of the concentration of the corresponding element, assuming the collection semiangle β of the spectrum is known. Extrapolation usually assumes a power-law energy dependence: AE^{-r}, where A and r are determined from least-squares fitting to the pre-edge background. The core-loss intensity is then integrated over an energy range Δ beyond the edge threshold; for $\Delta > 50$ eV, the near-edge fine structure is averaged out and the resulting integral $I_c(\beta, \Delta)$ represents the amount of the element, independent of its atomic environment (figure 22).

Although the angular distribution of scattering is a complicated mixture of elastic, plasmon and plural scattering, the *areal density* of the element (N atoms per unit area) can be estimated from the simple formula:

$$I_c(\beta, \Delta) \approx N I_l(\beta, \Delta)\sigma(\beta, \Delta). \tag{30}$$

If the local specimen thickness t is known, the elemental concentration n is given by $n = N/t$. The quantity $\sigma(\beta, \Delta)$ is a partial cross section, calculated for core-loss scattering up to an angle β and energy range Δ beyond the threshold. For K-shells, this cross section is available from the hydrogenic model (Egerton 1979); for other shells, Hartree–Slater calculations or experimental measurements are used (Rez 1982, Hofer 1987). The term $I_l(\beta, \Delta)$ in equation (30) represents an integral of the low-loss spectrum up to an energy loss Δ, including the entire zero-loss peak. Both I_c and I_l can be measured in arbitrary units since only their ratio is required to deduce N; there is no need to calibrate the recorded intensities or measure the electron-beam current. For typical values of t and β, equation (30) makes approximate allowance for elastic and plural-inelastic scattering (Egerton 1996).

As an example, Crozier (2007) used equation (30) to measure the amount of nitrogen, oxygen and silicon within a STEM probe focused onto a thin Si_3N_4 membrane in the presence of water vapour. Decrease in nitrogen and the development of an oxygen K-edge within a few seconds indicated the transformation of silicon nitride into silicon oxide. Using the latter as a nanolithography mask offers the possibility of patterning at 15 nm resolution.

Although equation (30) provides absolute (standardless) quantification, elemental ratios are often more useful. Applying equation (30) to two elements (A and B) and dividing gives

$$n^A/n^B = N^A/N^B$$
$$= [I_c^A(\beta, \Delta)/I_c^B(\beta, \Delta)][\sigma_c^B(\beta, \Delta)/\sigma_c^A(\beta, \Delta)]. \tag{31}$$

Since t and I_l cancel, neither the low-loss region nor the specimen thickness is needed to obtain the concentration ratio n^A/n^B.

Equation (30) also forms a basis for energy-selected imaging, where the aim is an *elemental map* showing the spatial distribution of a given element, the equivalent of an x-ray elemental map (Friel and Lyman 2006). Division of the I_c and I_l images roughly compensates for variations in elastic scattering (diffraction-contrast artefacts) although thickness variations still show up in the image. Alternatively, I_c can be displayed directly, provided the spectrum is recorded with a large collection aperture ($\beta > 50$ mrad) that admits most of the *elastic* scattering. With an aberration-corrected spectrometer and probe-forming lens, this simple procedure has been shown to provide elemental mapping down to the atomic scale; see figure 23.

The possibility of very high spatial resolution is one reason to prefer EELS to energy-dispersive x-ray spectroscopy (EDXS) as a method of elemental analysis in the TEM. Although EDXS provides a more convenient technique, avoiding the need for spectrometer alignment for example, its spatial resolution is limited to several nanometres as a result of x-rays generated by scattered electrons and stray electrons in the TEM column. Also the energy resolution of EDXS is currently ~100 eV, so the technique does not offer the kind of structural information that is available from EELS.

If the ratio of two core-loss signals is displayed, the result is an *elemental-ratio* image in which variations in specimen orientation, thickness and beam current are suppressed, according to equation (31). Dividing core-loss intensity by that of the preceding background gives a *jump-ratio image* showing the elemental distribution in a semi-quantitative way and with a better signal/noise ratio than an elemental map (Hofer *et al* 1995, Crozier 1995).

Accurate subtraction of the background from the core-loss signal is difficult in some cases: where the elemental concentration is low or where two ionization edges are

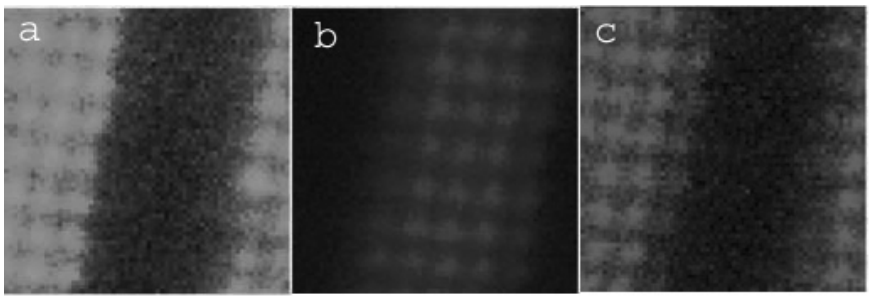

Figure 23. Atomic-scale elemental mapping: the 64 × 64-pixel images show columns of La, Ti, total and Mn atoms from (*a*) La-M, (*b*) Ti-L and (*c*) Mn-L edges recorded from $La_{0.7}Sr_{0.3}MnO_3$ by spectrum imaging. Reprinted from Muller *et al* (2008), courtesy of American Association for the Advancement of Science (AAAS).

separated in energy by less than 50 eV. It is then preferable to represent the spectrum as a power-law background (arising from a plasmon peak, for example) and core-loss profile for each edge:

$$J(E) = AE^{-r} + C_1 J_{c1}(E) + C_2 J_{c2}(E) + \cdots. \qquad (32)$$

The core-loss profiles can be calculated or (better) measured using elemental standards of known thickness and composition. The weightings (C_1, C_2, ...) of each contribution are adjusted by multiple least-squares (MLS) fitting and their values converted to relative concentrations, knowing an ionization cross section for each element (Leapman 2004a, Bertoni and Verbeeck 2008).

4.5. Spatial resolution of EELS

The spatial resolution of an energy-loss spectrum or an energy-filtered image depends on many factors (Egerton 2007). Some are instrumental and involve the electron optics of the TEM column; strongly excited lenses of small focal length (<2 mm) achieve low coefficients of spherical and chromatic aberration and a point resolution below 0.2 nm, while the aberration correction gives further improvement. However, such high performance is only meaningful when the TEM has highly stable power supplies and is operated in an environment where changes in magnetic field, ambient pressure and temperature changes are minimized by careful room design (Muller *et al* 2006).

Other resolution factors relate to the physics of electron scattering. Elastic scattering causes a broadening of a focused electron probe, by an amount that increases with specimen thickness (Goldstein *et al* 1977). Although this broadening limits the resolution of x-ray emission spectroscopy, the effective broadening is less for EELS if an angle-limiting aperture is used to eliminate electrons scattered through larger angles. Beam broadening is also less in a crystalline specimen, as a result of electron channelling down atomic columns (Loane *et al* 1988).

Although beam broadening can be minimized by using an ultrathin specimen, there is another factor that is independent of thickness and inherent to the inelastic scattering itself: *delocalization* of the scattering. Delocalization can be understood in a semi-quantitative way in terms of a single-scattering model, treating beam broadening as a separate effect

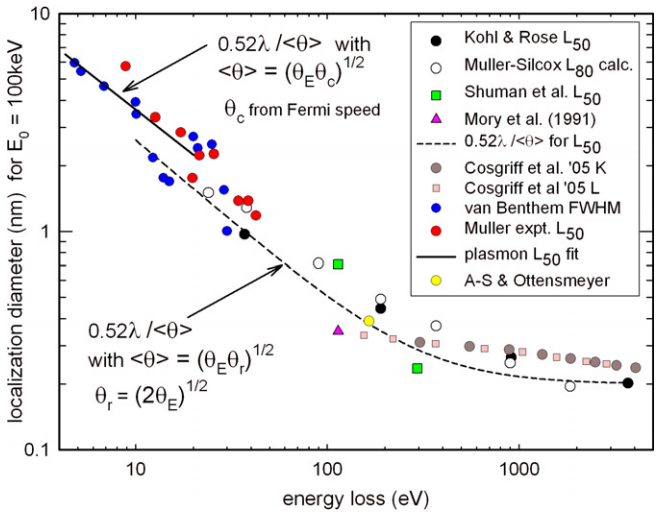

Figure 24. Delocalization of inelastic scattering as a function of energy loss, for 100 keV incident energy. The dashed curve shows equation (33) with median scattering angle evaluated from Bethe atomic scattering theory, solid line with $\langle\theta\rangle$ based on a plasmon model. From Egerton (2007), copyright Elsevier.

and regarding the delocalization distance L as a wave-optical resolution limit arising from the limited angular range of the inelastic scattering:

$$L_{50} = 0.52\lambda/\langle\theta\rangle. \qquad (33)$$

Equation (33) is essentially the Rayleigh criterion for resolution, with the factor 0.52 chosen to reflect the fact that L_{50} is a diameter containing 50% of the inelastic scattering; λ is the transmitted-electron wavelength and $\langle\theta\rangle$ is a median angle that contains 50% of the inelastic scattering, small enough so that $\langle\theta\rangle \approx \sin\langle\theta\rangle$ in the Rayleigh formula. For a Lorentzian angular distribution of inelastic scattering, $\langle\theta\rangle \approx (\theta_E\theta_c)^{1/2}$, where θ_c is the highest angle that reaches the electron detector. Equation (33) provides a fair approximation to both measurements and more exact calculations of the delocalization distance; see figure 24.

As seen in figure 24, delocalization amounts to 2–3 nm for plasmon losses, which could account for the fuzziness in figure 21. However, L_{50} falls with increasing energy loss (broader angular distribution) and is below 0.5 nm for $E > 100$ eV. This explains why, despite the low intensity, higher energy ionization edges are preferred when aiming for

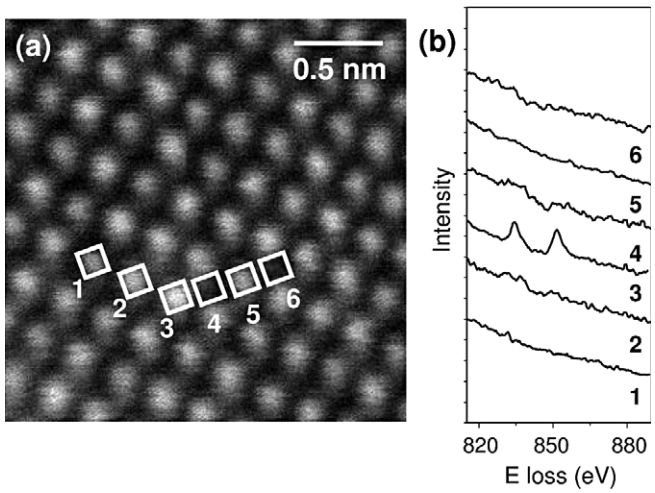

Figure 25. (*a*) Annular-dark-field *Z*-contrast STEM image of calcium titanate containing 4% La. (*b*) Core-loss spectra taken with the beam stationary at positions 1–6, demonstrating that the atomic column at 3 contained La, believed to be a single atom. Reprinted with permission from Varela *et al* (2004). Copyright (2004) by the American Physical Society.

atomic-resolution spectroscopic imaging (Kimoto *et al* 2007, Muller *et al* 2008).

M_{45}-edge (850 eV) spectra were used to identify which atomic columns contained lanthanum in ADF-STEM images of La-doped calcium titanate; see figure 25. Intensity simulations indicated that these columns contained only a single La atom. With the aid of electron-channelling calculations, it may even be possible to use the core-loss intensity to estimate the depth of each atom, thereby providing three-dimensional atomic imaging (Varela *et al* 2005).

The dashed curve in figure 24 assumes a Lorentzian angular distribution of core-loss scattering. If core losses well above an ionization-edge threshold are measured, $\langle\theta\rangle$ will approximate to the larger Bethe-ridge angle and the value of L_{50} is reduced (Kimoto *et al* 2008).

If the spectrometer collection aperture cuts off an appreciable part of the scattering, delocalization effects are more complicated. The Bethe atomic theory of scattering can be generalized to give the following expression for inelastic cross section:

$$\sigma = 2\pi m/(k_0 h^2) \int\int\int \psi_0^*(r,z) W(r,r') \psi_0(r',z)\, \mathrm{d}r\, \mathrm{d}r'\, \mathrm{d}z. \tag{34}$$

Here ψ_0 is a wavefunction of the incident electron; the integrations are over specimen thickness ($0 < z < t$) and over radial coordinates perpendicular to z. The function W is an effective *nonlocal* potential, related to the mixed dynamical form factor (Kohl and Rose 1985, Schattschneider *et al* 2000). It includes the effect of probe and detector geometry and is a function of two independent spatial coordinates (r and r'). As a result, equation (34) incorporates the effect of the phase of the transmitted electron and its diffraction by the specimen, making σ a sensitive function of the angle between the electron and the crystal. Calculations show that the inelastic intensity is not always proportional to the z-integrated current density, implying that energy-filtered STEM images cannot always be visually interpreted but require computer modelling to be understood on an atomic scale (Oxley and Pennycook 2008).

4.6. Magnetic measurements

The mixed dynamical form factor (MDFF) is also involved in recent attempts to use EELS to determine magnetic (electron-spin) properties of materials (Schattschneider *et al* 2008). This kind of measurement can be achieved using circularly polarized x-rays; but instead of using a spin-polarized electron source (whose intensity is weak), a regular TEM is used together with an energy-loss spectrometer or omega filter. The experiment involves measuring core-loss spectra at two carefully chosen locations in the diffraction plane. Under dynamical diffraction conditions, inelastic interference due to MDFF terms increases or decreases the electron intensity by several per cent (at the L_3 and L_2 white-line peaks of Co, Fe or Ni), dependent on the spin direction and the location of the detector in the diffraction plane. Subtraction of the two spectra then gives a signal of opposite sign at the two edges and although the signal is weak and noisy, a resolution down to 6 nm has been achieved for the L_{23} edges of Co. The aim is to apply this method to spintronic devices and achieve better spatial resolution than is possible from x-ray absorption measurements.

4.7. Radiation damage

In many materials, the practical limit to spatial resolution is set by radiation damage. For organic and some inorganic compounds, the damage mechanism is *radiolysis* (ionization damage): the breaking of chemical bonds as a result of inelastic scattering. Since this same scattering provides the EELS signal, the signal/damage ratio is independent of the accelerating voltage; damage occurs even for low-energy incident electrons, as used in HREELS (Chen *et al* 2003), although it is confined to the surface of the specimen. X-rays, used in XAS, also cause radiolysis, although for core-loss fine-structure studies the damage has been estimated to be a factor of several hundred less, depending on the width of the energy range analysed (Rightor *et al* 1997). This advantage arises because x-ray photons excite only the transitions being measured whereas electrons excite all energy losses simultaneously. X-ray damage is estimated (Henderson 1995) to be a factor of 10^3–10^4 *larger* than for electrons when the information being sought comes from *elastic* scattering (i.e. diffraction).

For metallic and semi-metallic specimens, there is no radiolysis but displacement damage (due to *elastic* scattering) occurs at high radiation dose. This process occurs only above a threshold incident energy, which is above 200 keV for medium-Z and heavier elements. However, the displacement of *surface* atoms (electron-beam *sputtering*) has a lower energy threshold (Egerton *et al* 2006b). Although the required electron dose is high, sputtering is expected to be quite rapid in a focused aberration-corrected electron probe, where the current density can exceed 10^6 A cm^{-2}.

Table 3. Electron dose to produce damage and the corresponding limit to spatial resolution, for 20 nm specimen thickness and 200 keV incident energy (Egerton 2007). The spread in D_c values corresponds to different specimen materials within each category. The last column relates to the detection of 10% calcium (at SNR = 5) from the L_{23}-edge.

Damage mechanism	Type of specimen	Damage dose D_c (C cm^{-2})	d (nm) for low-loss EELS	d (nm) for 350 eV-EELS
Radiolysis	Organic	10^{-3}–1	<0.5	1–300
Radiolysis	Inorganic	0.1–10^6	<0.05	0.01–30
Sputtering	Metallic	2000–40 000	$<5 \times 10^{-4}$	<0.2

Radiation damage limits the number of electrons incident on each resolution element of size d to $(D_c/e)d^2$, where e is the electronic charge and D_c a *critical* dose (charge per unit area) needed to cause the damage. The number of inelastically scattered electrons (the EELS signal) is therefore limited to $n \approx (t/L)(D_c/e)d^2$, where t is the specimen thickness and L is some effective MFP that depends on the specimen and the inelastic-scattering process involved. Associated with these n electrons is an electron-beam shot noise $n^{1/2}$, giving a signal/noise ratio SNR $= n/n^{1/2} = n^{1/2}$, assuming Poisson statistics where the standard deviation is the square root of the mean value. Combining the two expressions gives $(t/L)(D_c/e)d^2 = n = (\mathrm{SNR})^2$ and taking SNR $= 5$ (the so-called Rose criterion for visibility), the resolution limit imposed by radiation damage is

$$\mathrm{d} \approx 5(L/t)^{1/2}(e/D_c)^{1/2}. \tag{35}$$

Estimates of d are given in table 3, which shows that radiation damage sets the spatial-resolution limit ($d >$ atomic dimensions) for organic specimens and some inorganic compounds. For more radiation-resistant specimens, other factors (as discussed in section 4.5) are likely to be more important, except perhaps for core-loss spectroscopy using high-E edges (Egerton 1996).

Although radiation damage acts as a limitation to any electron-beam measurement, EELS offers a method of characterizing this damage for a particular type of specimen. Change in thickness (mass loss) can be monitored from the low-loss region and the loss of specific elements from ionization edges (Egerton 1996).

4.8. Use of chemical shifts and near-edge fine structure

The oxidation state of an element can be judged from the chemical shift or from the near-edge fine structure, such as the L_3/L_2 ratio in the case of a transition metal. Daulton *et al* (2003) used both techniques and plotted chromium L_3/L_2 ratios and L_3 threshold energy for a variety of inorganic compounds with Cr in oxidation states between 2 and 6. As seen in figure 26, the data cluster into groups, confirming a correlation between both types of measurement. They also examined *Shewanella oneidensis* bacteria, using an environmental cell that kept the specimen hydrated in the TEM and found that the resulting data fell into the Cr(III) region (see figure 26), confirming that these bacteria can be active sites for reduction in the toxic Cr(VI) species in chromium-contaminated water.

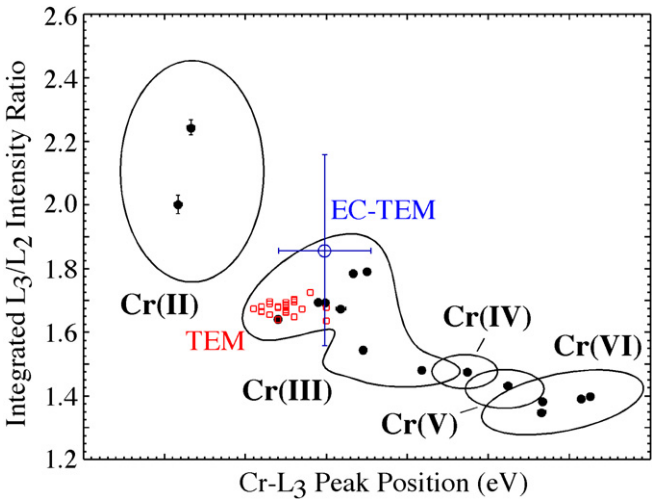

Figure 26. Chromium L_3/L_2 ratio plotted against L_3 threshold energy for inorganic compounds (data points within curved boundaries) and measured for *S. oneidensis* (central data point with large error bars). Reproduced from Daulton *et al* (2003), with permission of Cambridge University Press.

Energy-filtered (EFTEM) imaging has been used to plot L_3/L_2 ratios as an intensity map, in order to display variations in the valence state of Mn and Co in mixed-valence specimens (Wang *et al* 1999). The existence of a chemical shift must be considered when using core-loss spectroscopy to examine interfaces, for example, using the 'spatial difference' method (Muller *et al* 1998).

As integrated circuits become increasingly miniaturized, the thickness of the gate oxide in a field-effect transistor has fallen towards 1 nm in order to reduce gate voltage and power dissipation. Since this corresponds to only five Si atoms across, the properties of the oxide might be expected to depart considerably from the bulk values. High-resolution STEM of cross-sectional (XTEM) specimens, combined with core-loss EELS, provides a way of investigating these effects (Batson 1993). Figure 27 shows how the background-subtracted oxygen-K edge changes as the STEM probe approaches the Si interface from a native oxide. The threshold shifts downwards by 3 eV, indicating a reduced bandgap, and the sharp threshold peak disappears. This peak arises from backscattering of the ejected core electron from nearest-neighbour oxygen atoms (Si atoms backscatter much less than oxygen), so its absence close to the interface indicates a silicon-rich environment: a suboxide SiO_x where $x < 2$. Similar results were obtained for thermally grown oxide, as used in device fabrication. From the analysis of the two components

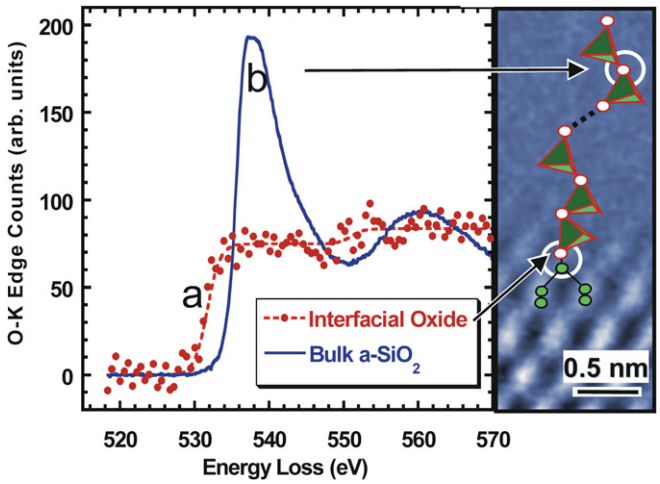

Figure 27. Oxygen K-loss spectra from the native oxide on silicon (solid line b) and from the region near the Si interface (data a). Reproduced from Muller *et al* (1999), with permission of Nature Publishing Group.

of the near-edge structure, the suboxide was estimated to have a width of 0.75 nm, out of a total thermal-oxide width of 1.6 nm (Muller *et al* 1999).

In general, the near-edge fine structure can give useful information on interatomic bonding (Browning *et al* 1997) but for quantitative results it is important to avoid edges that are strongly affected by the presence of the core hole, such as cations in ionic materials (Rez and Muller 2008). Principal-component analysis (PCA) is a useful technique for isolating the different fine-structure components present in a spectrum-image dataset and thereby produce a map showing chemical and bonding information. Since one of the components is random noise, this technique can also reduce the image noise without sacrificing spatial or energy resolution (Bosman *et al* 2006).

5. Conclusions

Within the last decade, TEM-based energy-loss spectroscopy has undergone steady development. Gun monochromators have become commercially available, making the TEM-EELS energy resolution comparable to that typical of XAS (∼0.1 eV). Partly for this reason, and also prompted by demands of the semiconductor industry and nanotechnology initiatives, more attention has been given to the low-loss region of the spectrum. This has led to renewed interest in the theory of surface-plasmon and Čerenkov losses in thin specimens, as first investigated by Kröger (1968). Core-loss spectroscopy has benefited from a better understanding of relativistic effects and of the delocalization of inelastic scattering in crystalline materials. Bayesian deconvolution techniques have been applied to both low-loss and core-loss regions with the aim of revealing additional fine structure. Taking advantage of such developments and of the improved stability of a modern TEM, EELS is being applied to the structural and chemical analysis of practical materials down to the atomic scale. Once instrumental limitations have been overcome, the ultimate spatial resolution is set by scattering delocalization and radiation damage to the specimen.

Future instrumental developments may include improved monochromator designs and the adoption of high-brightness electron sources, possibly based on carbon nanotubes (Fransen *et al* 1999). Another useful development would be an energy-loss spectrometer for transmission EELS and energy-filtered imaging in a scanning electron microscope (SEM). Because the SEM uses an accelerating voltage of 30 keV or lower, transmission measurements will be restricted to ultrathin specimens, such as nanotubes and nanoparticles. However, the low electron energy provides higher STEM-image contrast and makes it easier to achieve good energy resolution. With the addition of a suitable monochromator, it might be possible to achieve an energy resolution (∼10 meV) sufficient to examine vibrational modes of energy loss and to investigate the chemical bonding and phonon modes in nanostructures. After correction of lens aberrations, atomic resolution at 30 keV should be possible (Krivanek *et al* 2008).

Further information on the basic theory and practice of TEM-EELS is given in introductory form by Brydson (2001) in greater detail by Egerton (1996) and in two multi-author volumes edited by Reimer (1995) and Ahn (2004). Research papers on TEM-EELS are to be found in microscopy journals, particularly *Ultramicroscopy* and *Micron*, and scattered among various physics and materials science journals. A recent review by Spence (2006) is largely complementary to the present one, with more emphasis on STEM, channelling effects and applications to glasses and nanotubes. A short review of biophysical applications has been given by Leapman (2004b).

References

Ahn C C (ed) 2004 *Transmission Electron Energy Loss Spectrometry in Materials Science and the EELS Atlas* (New York: Wiley)

Ahn C C and Krivanek O L 1983 *EELS Atlas* (Warrendale, PA: Gatan Inc.); available from Gatan (www.gatan.com)

Alexander D T L, Crozier P A and Anderson J R 2008 Brown carbon spheres in East Asian outflow and their optical properties *Science* **321** 833–6

Barbarez M K, Das Gupta D K and Hayward D 1977 On the mechanisms of characteristic electron energy loss spectra of polymers *J. Phys. D: Appl. Phys.* **10** 1789–800

Batson P E 1993 Simultaneous STEM imaging and electron energy-loss spectroscopy with atomic column sensitivity *Nature* **366** 727–8

Batson P E 2008 Local crystal anisotropy obtained in the small probe geometry *Micron* **39** 648–52

Batson P E, Kavanah K L, Woodall J M and Mayer J M 1986 Electron-energy-loss scattering near a single misfit dislocation at the GaAs/GaInAs interface *Phys. Rev. Lett.* **57** 2719–32

Bertoni G and Verbeeck J 2008 Accuracy and precision in model based EELS quantification *Ultramicroscopy* **108** 782–90

Bosman M, Watanabe M, Alexander D T L and Keast V J 2006 Mapping chemical and bonding information using multivariate analysis of electron energy-loss spectrum images *Ultramicroscopy* **106** 1024–32

Brown L M 1997 A synchrotron in a microscope *Proc. EMAG97 (Cambridge) (Inst. Phys. Conf. Ser. 153)* pp 17–21

Browning N D, Wallis D J, Nellist P D and Pennycook S J 1997 EELS in the STEM: Determination of materials properties on the atomic scale *Micron* **28** 333–48

Browning N D, Arslan I, Bradley J P, Chi M, Dai Z, Erni R, Herrera M, Okamoto N L and Ramasse Q 2007 Aberration corrected and monochromated TEM/TEM for materials science *Microsc. Microanal.* **13** (Suppl 2) 1180–1 CD

Brydson R 2001 *Electron Energy Loss Spectroscopy* (Oxford: Bios)

Chen Y, Palmer R E, Shelley E J and Preece J A 2003 HREELS studies of gold nanoparticles with dialkyl sulphide ligands *Surf. Sci.* **502/503** 208–13

Crozier P A 1995 Quantitative elemental mapping of materials by energy-filtered imaging *Ultramicrosopy* **58** 157–74

Crozier P A 2007 Nanoscale oxide patterning with electron–solid–gas reactions *Nano Lett.* **7** 2395–8

Crozier P A and Egerton R F 1989 Mass thickness determination by Bethe-sum-rule normalization of the electron energy-loss spectrum *Ultramicroscopy* **27** 9–18

Daniels H R, Brydson R, Brown A and Rand B 2003 Quantitative valence plasmon mapping in the TEM: viewing *Ultramicroscopy* **96** 547–58

Daulton T L, Little B J and Lowe K 2003 Determination of chromium oxidation state in cultures of dissimilatory metal reducing bacteria by electron energy loss spectroscopy *Microsc. Microanal.* **9** (Suppl 2) 1480–1

Duscher G, Browning N D and Pennycook S J 1998 Atomic column resolved electron energy-loss spectroscopy *Phys. Status Solidi* A **166** 327–42

Eberlein T U, Bangert U, Nair R R, Jones R, Gass M, Bleloch A L, Novoselov K S, Geim A and Briddon P R 2008 Plasmon spectroscopy of free-standing graphene films *Phys. Rev.* B **77** 233406

Egerton R F 1979 K-shell ionization cross sections for use in microanalysis *Ultramicroscopy* **4** 169–79

Egerton R F 1996 *Electron Energy-Loss Spectroscopy in the Electron Microscope* 2nd edn (New York: Plenum/Springer)

Egerton R F 2007 Limits to the spatial, energy and momentum resolution of electron energy-loss spectroscopy *Ultramicroscopy* **107** 575–86

Egerton R F and Whelan M J 1974 The electron energy-loss spectrum and band structure of diamond *Phil. Mag.* **30** 739–49

Egerton R F, Qian H and Malac M 2006a Improving the energy resolution of x-ray and electron energy-loss spectra *Micron* **37** 310–15

Egerton R F, Wang F and Crozier P A 2006b Beam-induced damage to thin specimens in an intense electron probe *Microsc. Microanal.* **12** 65–71

Erni R and Browning N D 2008 The impact of surface and retardation losses on valence electron energy-loss spectroscopy *Ultramicroscopy* **108** 84–99

Fano U 1956 Differential inelastic scattering of relativistic charged particles *Phys. Rev.* **102** 385–7

Frank J 2007 *Electron Tomography: Three-Dimensional Imaging with the Transmission Electron Microscope* 2nd edn (New York: Plenum)

Fransen M J, van Rooy T L and Kruit P 1999 Field emission energy distribution from individual multi-walled carbon nanotubes *Appl. Surf. Sci.* **146** 312–27

French R H, Muellejans H, Jones D J, Duscher G, Cannon R M and Ruehle M 1998 Dispersion forces and Hamaker constants for intergranular films in silicon nitride from spatially resolved-valence electron energy loss spectrum imaging *Acta Mater.* **46** 2271–87

Friel J J and Lyman C E 2006 X-ray mapping in electron-beam instruments *Microsc. Microanal.* **12** 2–25

Garcia de Abajo F J and Echenique P M 1992 Wake potential formation in a thin foil *Phys. Rev.* B **45** 8771–4

Gass M H, Koziol K, Windle A H and Midgley P A 2006 Four-dimensional spectral tomography of carbonaceous nanocomposites *Nano Lett.* **6** 376–9

Gilman J 1999 Plasmons at shock fronts *Phil. Mag.* **79** 643–54

Gloter A, Douiri A, Tence M, Imhoff D and Colliex C 2003 Improving energy resolution of EELS spectra: an alternative to the monochromator solution *Ultramicroscopy* **96** 385–400

Goldstein J I, Costley J L, Lorimer G W and Reed S J B 1977 Quantitative analysis in the electron microscope *Scanning Electron Microscopy Part 1* (Chicago: ITRI) pp 315–24

Haider M, Uhlemann S, Schwan E, Rose H, Kabius B and Urban K 1998 Electron microscopy image enhanced *Nature* **392** 768–9

Hébert C, Schattschneider P, Franco P H and Jouffrey B 2006 ELNES at magic angle conditions *Ultramicroscopy* **106** 1139–43

Hébert C 2007 Practical aspects of running the WIEN2k code for electron spectroscopy *Micron* **38** 12–28

Henderson R 1995 The potential and limitations of neutrons, electrons and x-rays for atomic resolution microscopy of unstained biological molecules *Q. Rev. Biophys.* **28** 171–93

Hofer F 1987 EELS quantification of M edges by using oxidic standards *Ultramicroscopy* **21** 63–8

Hofer F, Warbichler P and Grogger W 1995 Characterization of nanometer sized precipitates in solids by electron spectroscopic imaging *Ultramicroscopy* **59** 15–31

Howie A 1983 Surface reactions and excitations *Ultramicroscopy* **11** 141–8

Hu X, Sun Y and Yuan J 2007 Multivariate statistical analysis of electron energy-loss spectroscopy in anisotropic materials *Ultramicroscopy* **108** 465–71

Iakoubovskii K, Mitsuishi K, Nakayama Y and Furuya K 2008a Thickness measurements with electron energy loss spectroscopy *Microsc. Res. Tech.* **71** 616–31

Iakoubovskii K, Mitsuishi K, Nakayama Y and Furuya K 2008b Mean free path of inelastic electron scattering: material dependence *Phys. Rev.* B **77** 104102

Ibach H and Mills D L 1982 *Electron Energy-Loss Spectroscopy and Surface Vibrations* (New York: Academic)

Inokuti M 1971 Inelastic collisions of fast charged particles with atoms and molecules—The Bethe theory revisited *Rev. Mod. Phys.* **43** 297–343

Inokuti M *et al* 1978 Inelastic collisions of fast charged particles with atoms and molecules—The Bethe theory revisited *Rev. Mod. Phys.* **50** 23–35 (addendum)

Itskovsky M A, Cohen H and Maniv T 2008 Far-field interaction of focused relativistic electron beams in electron energy loss spectroscopy of nanoscopic platelets *Phys. Rev.* B **78** 045419

Jeanguiillaume C and Colliex C 1989 Spectrum-image: the next step in EELS digital acquisition and processing *Ultramicroscopy* **78** 252–7

Johnson D W and Spence J C H 1974 Determination of the single-scattering probability distribution from plural-scattering data *J. Phys. D: Appl. Phys.* **7** 771–80

Jouffrey B, Schattschneider P and Hebert C 2004 The magic angle: a solved mystery *Ultramicroscopy* **102** 61–6

Keast V J 2005 Ab initio calculations of plasmons and interband transitions in the low-loss electron energy-loss spectrum *J. Electron Spectrosc. Relat. Phenom.* **143** 97–104

Keil P 1968 Elektronen-Energieverlustmessungen und Berechnung optischer Konstanten. II. Kaliumbromid *Z. Phys.* **214** 266–84

Kimoto K and Matsui Y 2002 Software techniques for EELS to realize about 0.3 eV energy resolution using 300 kV FEG-TEM *J. Microsc.* **208** 224–8

Kimoto K, Ishizuka K, Mizuguchi T, Tanaka I and Matsui Y 2003 The study of Al-L23 ELNES with resolution-enhancement software and first-principles calculation *J. Electron Microsc.* **36** 299–303

Kimoto K, Asaka T, Nagai T, Saito M, Matsui Y and Ishizuka K 2007 Element-selective imaging of atomic columns in a crystal using STEM and EELS *Nature* **450** 702–4

Kimoto K, Ishizuka K and Matsui Y 2008 Decisive factors for realizing atomic-column resolution using STEM and EELS *Micron* **39** 257–62

Klie R F, Zhu Y, Schneider G and Tafto J 2003 Experimental probing of the anisotropy of the empty p states near the Fermi level in MgB_2 *Appl. Phys. Lett.* **82** 4316–8

Koch E E and Otto A 1969 Characteristic energy losses of 30 keV electrons in vapours of aromatic hydrocarbons *Opt. Commun.* **1** 47–9

Kohl H and Rose H 1985 Theory of image formation by inelastically scattered electrons in the electron microscope *Adv. Electron. Electron Phys.* **65** 175–200

Krause M O and Oliver J H 1979 Natural widths of atomic K and L levels *J. Phys. Chem. Ref. Data* **8** 128–43

Krishman V and Ritchie R H 1970 Anomalous damping of volume plasmons in polycrystalline materials *Phys. Rev. Lett.* **24** 1117–9

Krivanek O L, Dellby N and Lupini A R 1999 Towards sub-Å electron beams *Ultramicroscopy* **78** 1–11

Krivanek O L, Dellby N, Keyse R J, Murfitt M F, Own C S and Szilagyi Z S 2008 Advances in aberration-corrected STEM and EELS *Advances in Imaging and Electron Physics* ed P W Hawkes (Amsterdam: Elsevier)

Kröger E 1968 Berechnung der energieverluste schneller elektronen in dünnen schichten mit retardierung *Z. Phys.* **216** 115–35

Lazar S, Botton G A, Wu M-Y, Tichelaar F D and Zandbergen H W 2003 Materials science applications of HREELS in near edge structure analysis and low-energy loss spectroscopy *Ultramicroscopy* **96** 535–46

Lazar S, Botton G A and Zandbergen H W 2006 Enhancement of resolution in core-loss and low-loss spectroscopy in a monochromated microscope *Ultramicroscopy* **106** 1091–103

Leapman R D 2004a EELS Quantitative analysis *Transmission Electron Energy Loss Spectrometry in Materials Science and The EELS Atlas* 2nd edn ed C C Ahn (Weinheim: Wiley-VCH) pp 49–96

Leapman R D 2004b Novel techniques in electron microscopy *Curr. Opin. Neurobiol.* **14** 591–8

Leapman R D, Fejes P L and Silcox J 1983 Orientation dependence of core edges from anisotropic materials determined by inelastic scattering of fast electrons *Phys. Rev.* B **28** 2361–73

Lenz F 1954 Zur Streuung mittelschneller Elektronen in kleinste Winkel *Z. Naturfrosch.* **9A** 185–204

Loane R F, Kirkland E J and Silcox J 1988 Visibility of single heavy atoms on thin crystalline silicon in simulated annular dark-field STEM images *Acta Crystallogr.* A **44** 912–27

Møller C 1932 Zur theorie des durchgangs schneller elektronen durch *Mater. Ann. Phys. Lpz.* **14** 531–85

Moreno M S, Lazar S, Zandbergen H W and Egerton R F 2006 Accuracy of the calculated unoccupied states in GaN phases as tested by high-resolution electron energy-loss spectroscopy *Phys. Rev.* B **73** 073308

Moreno M S, Jorissen K and Rehr J J 2007 Practical aspects of electron energy-loss spectroscopy (EELS) calculations using FEFF8 *Micron* **38** 1–11

Muller D A 1999 Why changes in bond lengths and cohesion lead to core-level shifts in metals, and consequences for the spatial difference method *Ultramicroscopy* **78** 163–74

Muller D A, Singh D J and Silcox J 1998 Connections between the electron energy-loss spectra, the local electronic structure, and the physical properties of a material: a study of nickel aluminum alloys *Phys. Rev.* B **57** 8181–202

Muller D A, Sorsch T, Moccio S, Baumann F H, Evans-Lutterodt K and Timp G 1999 The electronic structure at the atomic scale of ultrathin gate oxides *Nature* **399** 758–61

Muller D A, Kirkland E J, Thomas M G, Grazul J L, Fitting L and Weyland M 2006 Room design for high-performance electron microscopy *Ultramicroscopy* **106** 1033–40

Muller D A, Kourkoutis L F, Murfitt M, Song J H, Hwang H Y Silcox J, Dellby N and Krivanek O L 2008 Atomic-scale chemical imaging of composition and bonding by aberration-corrected microscopy *Science* **319** 1073

Nehayah J, Kociak M, Stéphan O, Garcia de Abajo F J, Tencé M, Henrard L, Taverna D, Pastoriza-Santos I, Liz-Marzán L M and Colliex C 2007 Mapping surface plasmons on a single metallic nanoparticle *Nat. Phys.* **3** 348–52

Oleshko V P and Howe J M 2007 In situ determination and imaging of physical properties of metastable and equilibrium precipitates using valence electron energy-loss spectroscopy and energy-filtering transmission electron microscopy *J. Appl. Phys.* **101** 054308

Overwijk M H F and Reefman D 2000 Maximum-entropy deconvolution applied to electron energy-loss spectroscopy *Micron* **31** 325–31

Oxley M P and Pennycook S J 2008 Image simulation for electron energy loss spectroscopy *Micron* **39** 676–84

Powell C J 1968 Characteristic energy losses of 8-keV electrons in liquid Al, Bi, In, Ga, Hg and Au *Phys. Rev.* **175** 972–82

Powell C J and Swan J B 1960 Effect of oxidation on the characteristic loss spectra of aluminum and magnesium *Phys. Rev.* **118** 640–3

Raether H 1980 *Excitation of Plasmons and Interband Transitions by Electrons* (Berlin: Springer)

Rafferty B and Brown L M 1998 Direct and indirect transitions in the region of the band gap using electron-energy-loss spectroscopy *Phys. Rev.* B **58** 10326–37

Reimer L ed 1995 *Energy-Filtering Transmission Electron Microscopy* (Berlin: Springer)

Rez P 1982 Cross sections for energy-loss spectrometry *Ultramicroscopy* **9** 283–8

Rez P and Muller D A 2008 The theory and interpretation of electron energy loss near-edge fine structure *Annu. Rev. Mater. Res.* **38** 18.1–18.24

Rightor E G, Hitchcock A P, Ade H, Leapman R D, Urquhart S G, Smith A P, Mitchell G, Fischer D, Shin H J and Warwick T 1997 Spectromicroscopy of poly(ethylene terephthalate): comparison of spectra and radiation damage rates in x-ray absorption and electron energy loss *J. Phys. Chem.* B **101** 1950–60

Ritchie R H 1957 Plasmon losses by fast electrons in thin films *Phys. Rev.* **106** 874–81

Sayers D E, Stern E A and Lytle F W 1971 New technique for investigating non-crystalline structures: Fourier analysis of the extended x-ray absorption fine structure *Phys. Rev. Lett.* **27** 1204–7

Schattschneider P, Nelhiebel M, Souchay H and Jouffrey B 2000 The physical significance of the mixed dynamic form factor *Micron* **31** 333–45

Schattschneider P, Hébert C, Franco H and Jouffrey B 2005 Anisotropic relativistic cross sections for inelastic electron scattering, and the magic angle *Phys. Rev.* B **72** 045142

Schattschneider P, Rubino S, Stoeger-Pollach M, Hébert C, Rusz J, Calmels L and Snoeck E 2008 Energy loss magnetic chiral dichroism: a new technique for the study of magnetic properties in the electron microscope *J. Appl. Phys.* **103** 07D931

Sorini A P, Rehr J J and Levine Z H 2008 Magic angle in electron energy loss spectra: relativistic and dielectric corrections *Phys. Rev.* B **77** 115126

Spence J C H 2006 Absorption spectroscopy with sub-angstrom beams: ELS in STEM *Rep. Prog. Phys.* **69** 725–58

Stern E A and Ferrell R A 1960 Surface plasma oscillations in a degenerate electron gas *Phys. Rev.* **120** 130–6

Stöger-Pollach M 2008 Optical properties and bandgaps from low loss EELS: pitfalls and solutions *Micron* **39** 1092–110

Stöger-Pollach M, Franco H, Schattschneider P, Lazar P S, Schaffer B W, Grogger B W and Zandbergen H W 2006

Čerenkov losses: A limit for bandgap determination and Kramers–Kronig analysis *Micron* **37** 396–402
Sun Y and Yuan J 2005 *Phys. Rev.* B **71** 125109
Sun S, Shi S and Leapman R 1993 Water distributions of hydrated biological specimens by valence electron energy loss spectroscopy *Ultramicroscopy* **50** 127–39
Sun Y and Yuan J 2005 Electron energy loss spectroscopy of core-electron excitation in anisotropic systems: magic angle, magic orientation, and dichroism *Phys. Rev.* B **71** 125109
Tiemeijer P C 1999 Operation modes of a TEM monochromator *Inst. Phys. Conf. Ser. 161* pp 191–4
Varela M *et al* 2004 Spectroscopic imaging of single atoms within a bulk solid *Phys. Rev. Lett.* **92** 095502
Varela M, Lupini A R, van Benthem K, Borisevich A Y, Chisholm M F, Shibata N, Abe E and Pennycook S J 2005 Materials characterization in the aberration-corrected scanning transmission electron microscope *Annu. Rev. Mater. Res.* **35** 539–69
Wang F, Egerton R F, Malac M, McLeod R A and Moreno M S 2008a The spatial resolution of electron energy-loss and x-ray absorption fine structure *J. Appl. Phys.* **104** 034906
Wang J, Li Q, Peng L-M and Malac M 2008b The dielectric response of the $H_2Ti_3O_7$ nanotube investigated by valence electron energy loss spectroscopy *Appl. Phys. Lett.* at press
Wang Z L, Bentley J and Evans N D 1999 Mapping the valence states of transition-metal elements using energy-filtered transmission electron microscopy *J. Phys. Chem.* B **103** 751–3
Yurtsever A, Weyland M and Muller D A 2006 Three-dimensional imaging of nonspherical silicon nanoparticles embedded in silicon oxide by plasmon tomography *Appl. Phys. Lett.* **89** 151920
Zhang L, Erni R, Verbeek J and Van Tenderloo G 2008 Retrieving the dielectric function of diamond from valence electron energy-loss spectroscopy *Phys. Rev.* B **77** 195119